Structure-based mechanism of RyR channel operation by calcium and magnesium ions

Alexandra Zahradníková[1]✉, Jana Pavelková[1], Miroslav Sabo[2], Sefer Baday[3], and Ivan Zahradník[1]✉

[1] Department of Cellular Cardiology, Institute of Experimental Endocrinology, Biomedical Research Center, Slovak Academy of Sciences, Bratislava, Slovakia. [2] Bioinformatics Laboratory, Biomedical Research Center, Slovak Academy of Sciences, Bratislava, Slovakia. [3] Applied Informatics Department, Informatics Institute, Istanbul Technical University, Istanbul, Türkiye.

✉ Corresponding authors:

Alexandra Zahradníková, alexandra.zahradnikova@savba.sk

Ivan Zahradník, ivan.zahradnik@savba.sk

Short title: RyR channel operation by divalent ions

Abstract

Ryanodine receptors (RyRs) serve for excitation-contraction coupling in skeletal and cardiac muscle cells in a noticeably different way, not fully understood at the molecular level. We addressed the structure of skeletal (RyR1) and cardiac (RyR2) isoforms relevant to the gating by divalent ions (M^{2+}). The bioinformatics analysis of 43 cryo-EM RyR structures ascertained the EF1 and EF2 loops as a moderate-affinity non-specific M^{2+} binding site interacting with the S23 loop of neighbor monomer stronger in RyR1 than RyR2. The EF1/EF2 loops were allosterically coupled to the S6 gate by two parallel pathways. The intra-monomeric pathway uses the U-motif, ATP binding site, S45 linker, and S6 helix, shared with the Ca^{2+}-activation pathway in both RyR isoforms. The inter-monomeric pathway, prominent in RyR1, passes through the S23* loop of the neighbor monomer (*) and *via* the U-motif* to the S6* gate either directly or through the S45* linker or CFF* binding site. The structural pieces of evidence for the M^{2+}-binding activation and inhibition sites and their interacting allosteric networks were implemented in the model of RyR operation based on statistical mechanics, MWC theorem, and Markov processes. This model defines allosterically coupled closed, open, and inactivated RyR macrostates common for both RyR isoforms and solves the relative occupancy of macrostates in dependence on cytosolic M^{2+} concentrations. The model approximated the single-channel open probability data for RyR1 and RyR2 of several species obtained in the presence or absence of ATP and luminal calcium. The proposed platform of RyR operation interprets the structural and functional data of mammalian RyR channels on common grounds.

Keywords:

RyR channel; striated muscle; structure-function; ion-binding site; allosteric pathway; open probability; activation; inactivation.

Introduction

Ryanodine receptor (RyR) plays a central role in the calcium-dependent functions of excitable cells. RyRs reside on the membrane of the endoplasmic/sarcoplasmic reticulum (ER/SR) and upon cell excitation, they control the release of calcium ions from the ER/SR lumen to cytosol. Three RyR isoforms are expressed in mammals: RyR1 in skeletal muscle cells, RyR2 in cardiomyocytes, neurons, and endocrine cells, and RyR3 in many tissues at lower levels (Meissner, 2017). Although RyR isoforms differ substantially in their sequence, function, and role in different tissue types, they show almost identical molecular architecture (Wagenknecht and Samso, 2002). All three RyR isoforms form a homo-tetrameric transmembrane channel, which harbors multiple regulatory sites, mostly at their cytosolic side (Meissner, 2017). It is important to note that, with a few exceptions, the regulatory binding sites reside on the monomer, so there are 4 equivalent binding sites of each type per RyR tetramer. Consequently, individuals heterozygous for a congenital mutation in the RyR gene have an equal abundance of mutated and wild-type monomers, which combine at random into tetramers (Zahradnik et al., 2005; Wilson et al., 2021).

Specific ligand-binding sites have been found for natural activators Ca^{2+}, ATP, and xanthines (des Georges et al., 2016; Chi et al., 2019; Melville et al., 2022a; Miotto et al., 2022); for regulatory molecules like calstabins and calmodulin (des Georges et al., 2016; Gong et al., 2019; Woll et al., 2021), the diamide insecticide chlorantraniliprole (Ma et al., 2020); and for emerging clinically important stabilizers like Rycals (Melville et al., 2022a; Miotto et al., 2022). RyR activators ryanodine and imperacalcin have binding sites on the conduction pathway common to the whole RyR tetramer (des Georges et al., 2016; Haji-Ghassemi et al., 2023). Many other regulatory sites need to be revealed for regulators such as dantrolene, junctin, triadin, luminal Ca^{2+}, calsequestrin, etc. The modulation of RyR activity by phosphorylation, oxidation, nitrosylation, etc., is of importance but only the effects of PKA phosphorylation on RyR2 structure have been studied up to date (Miotto et al., 2022).

The molecular architecture as well as the localization of mutations that compromise RyR function is very similar among isoforms. Most known mutations cause muscle conditions that may have fatal consequences in the case of cardiac muscle (Robinson et al., 2006; Sleiman et al., 2021). Over two hundred mutations that cause dysregulation of calcium release are localized mainly in four specific regions of the RyR monomer (Ikemoto and Yamamoto, 2000; Robinson et al., 2006; George et al., 2007; Iyer et al., 2023). These mutations are typically characterized by the increased sensitivity of calcium release to cytosolic and/or luminal calcium, by the decreased sensitivity to inactivation by high cytosolic concentrations of magnesium or calcium, or by increased basal RyR activity (Lehnart et al., 2004; Witherspoon and Meilleur, 2016; Guo et al., 2020; Sleiman et al., 2021; Wilson et al., 2021).

The complex structure of RyR tetramer may adopt a large number of configurations (des Georges et al., 2016; Dashti et al., 2020). In RyR1, four discrete structural states were discerned under different cytosolic conditions - closed (C), primed (P), open (O), and inactivated (I) (des Georges et al., 2016; Nayak and Samso, 2022; Nayak et al., 2024). With increasing concentrations of the activators (Ca^{2+}, ATP derivatives, or xanthine derivatives), the configuration of the tetramers shifted from the closed state to the primed and open state (des Georges et al., 2016; Dashti et al., 2020). At a very high Ca^{2+} or Mg^{2+} concentration, the inactivated state was observed (Nayak and Samso, 2022; Nayak et al., 2024). Under

similar conditions, analogous C, P, and O states were observed also in RyR2 (Chi et al., 2019); unfortunately, the structure of RyR2 in the inactivated state has not been published yet. Upon transition from the closed state to either primed, open, or inactivated states, the large cytoplasmic shell moves downward and outward (des Georges et al., 2016; Steele and Samso, 2019; Miotto et al., 2022), a movement that transpires as a progressively more negative flexion angle (Steele and Samso, 2019), and the Central and C-terminal domains rotate against each other in each monomer (Nayak and Samso, 2022). The overall structure of the primed and inactivated states resembles more the open than the closed state but the ion conduction pore is closed (des Georges, 2016 #5; Chi, 2019 #15; Nayak, 2022 #48).

In striated muscle cells, RyR channels cluster at discrete sites of sarcoplasmic reticulum attached to the sarcolemma where electrical excitation triggers transient calcium release by activation of RyRs. Activation mechanisms differ between skeletal and cardiac muscle cells. *In situ*, RyR1 channels are open by direct coupling to the $Ca_v1.1$ channels, while RyR2 channels are activated by binding calcium ions injected through the $Ca_v1.2$ channels (Rios and Stern, 1997). In isolation, however, the RyR1 and RyR2 channels are activated by Ca^{2+} ions equally well (Chu et al., 1993). The termination of RyR activity in situ is not fully understood (Schneider and Simon, 1988; Stern, 1992; Stern et al., 1997). In skeletal muscle cells, calcium-dependent inactivation of RyR1 is generally accepted as the major termination mechanism (Schneider and Simon, 1988). In cardiac muscle cells, the termination of RyR activity is less clear since the calcium-dependent RyR2 inactivation is weaker than that of RyR1; nevertheless, divalent ions (M^{2+}) are involved in the RyR2 inactivation/inhibition as well (Gillespie and Fill, 2013; Laver et al., 2013; Niggli et al., 2013; Gillespie, 2020; Iaparov et al., 2022).

In both RyR1 and RyR2 isoforms, Mg^{2+} ions decrease the intensity of calcium release in a concentration-dependent manner. In isolated RyRs, Mg^{2+} ions lead to an increase of the EC50 and a reduction of the maximum of RyR activation by Ca^{2+} (Laver et al., 1997; Zahradnikova et al., 2003; Iaparov et al., 2022). Ca^{2+} and Mg^{2+} have a similar inhibitory potency on the open probability in both RyR1 and RyR2 (Laver et al., 1997). This indicates the presence of a non-specific divalent ion-binding site in the RyR structure. Recently, mathematical modeling of the cardiac calcium release site (Iaparov et al., 2022) confirmed that Mg^{2+} ions could at the same time act as the negative competitor at the calcium activation site and as an inhibitor at the inhibition site. Unfortunately, the structural counterpart of RyR inactivation, an inhibitory binding site for divalent ions, has not been located yet in RyR structures.

The activation of RyR by agonists was shown to be accompanied by a conformational change around the Ca^{2+} binding site that leads to a decrease in the free energy and to a concomitant increase of the Ca^{2+} binding affinity and a population shift between the closed and open conformations (Dashti et al., 2020). It should be pointed out that the activation mechanism of both RyR1 and RyR2 by calcium is fundamentally identical regarding the Ca^{2+} dependence of their open probability (Chu et al., 1993). The amino acid identity and 3D configuration of binding sites for Ca^{2+}, ATP, and caffeine/xanthine are equivalent in both RyR isoforms (des Georges et al., 2016; Chi et al., 2019).

Though RyRs have similar activation mechanisms, they have different inactivation mechanisms. The single-channel activity of RyR1 was inhibited by Ca^{2+} at a much lower concentration than that of RyR2 (Chu et al., 1993; Laver et al., 1995; Gyorke and Gyorke, 1998). Single-channel experiments provided the

118 same concentration dependence of the RyR inhibition for both Mg^{2+} and Ca^{2+} ions (M^{2+}), but a
119 substantially lower degree of inhibition in RyR2 than in RyR1 channels (Laver et al., 1997)). These
120 characteristics are opposite to the corresponding characteristics of RyR activation. Consequently, the
121 underlying structures and mechanisms are expected to be principally different, which is puzzling since
122 the equivalent components of RyR isoforms are similar. Moreover, the pore of the RyR tetramer is lined,
123 limited, and gated by the quadruplet of S6 segments; thus, one gating site executes both the activation
124 and the inactivation. Obviously, there is a paradox in RyR channels that equivalent structures execute
125 the activation similarly but the inactivation differently in RyR1 and RyR2.

126 In the structural context, the location of the divalent ion-binding RyR inhibition site has not been
127 revealed yet. Several candidate amino acid sequences were identified in the divergent region
128 (Sorrentino and Volpe, 1993) but later disproved as the inhibition site (Du and Maclennan, 1999; Perez
129 et al., 2003; Fessenden et al., 2004). Nevertheless, the exchange of the wild-type C-terminal quarter of
130 rabbit RyR1 for that of RyR2 shifted the inhibitory constant (IC50) of the calcium dependence of ^{3}H-
131 ryanodine binding close to the value of WT RyR2 (Du and Maclennan, 1999), thus the C-terminal quarter
132 has to contain the Ca-binding inhibitory site. This quarter encompasses also several other regulatory
133 domains (Figure 1), namely, the Central domain participating in the Ca^{2+} binding activation site; the C-
134 terminal domain that bears several residues of Ca-, ATP- and caffeine-binding activation sites; the U-
135 motif that participates at the ATP- and caffeine-binding sites; the EF-hand region with the putative Ca-
136 binding pair EF1 and EF2; and the S23 loop that bears one residue of the caffeine-binding site and two
137 residues interacting with the EF-hand region of a neighboring monomer (Samso, 2017; Hadiatullah et al.,
138 2022). Further experiments suggested the involvement of the EF-hand region in binding Ca ions and
139 inactivating RyR channels. The expressed and purified EF-hand regions of rabbit RyR1 and RyR2 bound
140 two Ca^{2+} ions with a similar, ≈50 µM affinity, as determined by equilibrium binding dialysis of ^{45}Ca (Xiong
141 et al., 1998). MD simulations of the membrane-embedded rabbit RyR1 C-terminal quarter showed the
142 Ca^{2+} binding ability of the EF-hand region, especially residues 4116-4119 of EF2 (Zheng and Wen, 2020).
143 The rRyR1 segment containing the EF1 motif (4017 – 4098) was suggested to be involved in inactivation
144 since its replacement with the corresponding RyR2 sequence in HEK cell-expressed RyR chimeras
145 increased IC50 of the ^{3}H-ryanodine binding inhibition from 1.1 mM to 3.8 mM Ca^{2+} (Gomez and
146 Yamaguchi, 2014). On the other hand, the replacement of the RyR1 EF2 sequence for its RyR2
147 counterpart did not have a significant effect on the inhibition of ^{3}H-ryanodine binding by Ca^{2+} (Gomez
148 and Yamaguchi, 2014). Additionally, scrambling of the EF1 hand calcium-binding loop in RyR1 also
149 increased the IC50 for calcium from 0.85 to 1.82 mM (Fessenden et al., 2004). Unfortunately, scrambling
150 of the EF2 calcium-binding loop canceled ^{3}H-ryanodine binding in RyR1, thus the role of EF2 in RyR
151 inactivation could not be clarified in those experiments (Fessenden et al., 2004).

152 Recent studies reporting RyR structure at a high calcium concentration provide only partial support for
153 the molecular mechanism of calcium-dependent inactivation. Wei et al. (2016) observed in RyR1 a
154 smaller E-F angle of the EF1 hand in the presence of 100 µM Ca^{2+} than in the absence of calcium. The
155 RyR1 structures 7tdg, 7tdi, 7tdj, and 7tdk determined at 3.7 mM Ca^{2+} were proposed to represent the
156 inactivated state since they showed the conduction pore closed (diameter of ≈11 Å at Cα atoms of
157 I4937) (Nayak and Samso, 2022). Importantly, the 7tdh structure obtained in parallel under the same
158 conditions showed the pore open (diameter of 14.3 Å) (Nayak and Samso, 2022) indicating that RyR may
159 attain two different states under the same conditions. This could explain in part why the RyR2 structure

6jiy obtained at 5 mM Ca^{2+} had the pore open (diameter of 17 Å) (Gong et al., 2019), at odds with the expectation to find the channel in the inactivated state with a closed pore at so high Ca^{2+} concentration. Confoundingly, even at 3.7 mM Ca^{2+} or 5-10 mM Mg^{2+} concentrations in the reconstitution media the Ca or Mg atoms were observed only at the Ca-activation site, near the bound ATP molecule, or in the ion flux pathway of RyR1 but not elsewhere (Nayak and Samso, 2022; Nayak et al., 2024). This indicates that the potential inhibition site has an affinity for divalent ions smaller than ATP (K_d ≈200 µM, (Bers et al., 1994)).

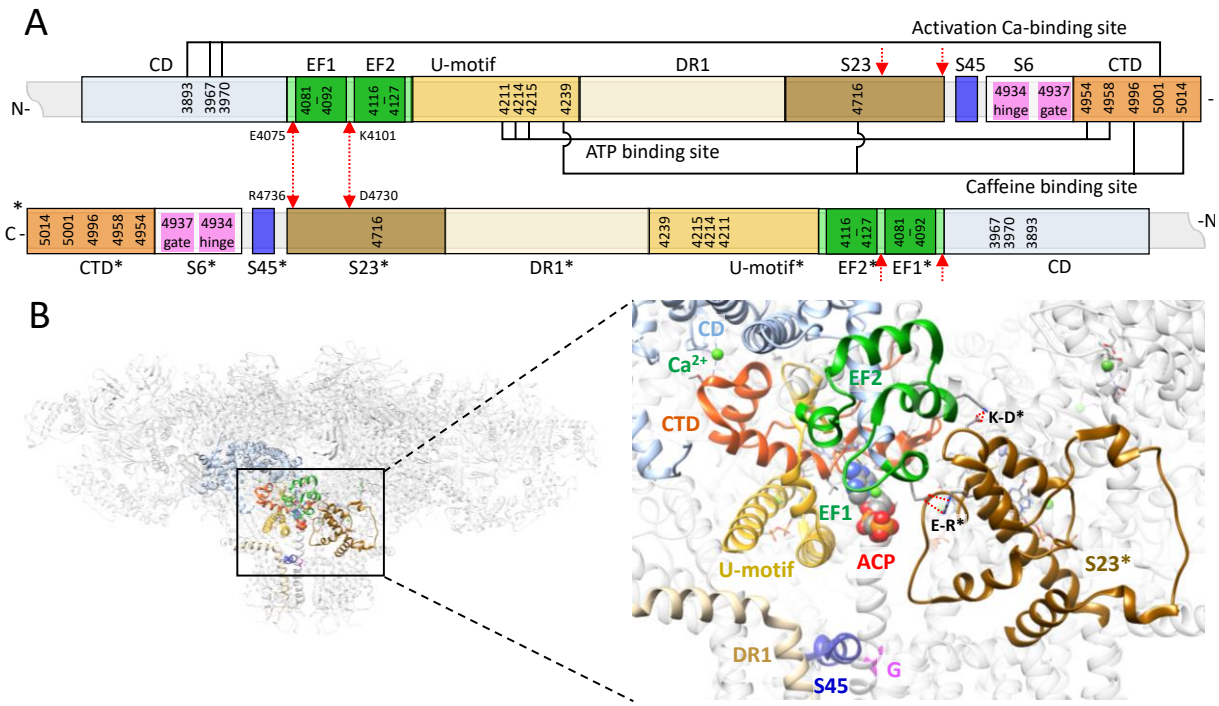

Figure 1. The sequences and the molecular structures related to the RyR channel operation.
A: The block scheme of the rRyR1 C-terminal quarter (3667-5037) for two neighbor monomers. Light blue - the Central domain (CD); light green - the EF-hand region; dark green - EF1 and EF2 motifs; tan – the Divergent region 1 (DR1); yellow - U-motif; light brown - S23 loop; blue – S45 linker (S45); white - the S6 segment with the hinge and gate residues in magenta; orange - the C-terminal domain (CTD). Red arrows – salt bridges between interacting residues of the EF-hand region and the S23* loop. The asterisks indicate a reference to the neighbor RyR monomer located counterclockwise in the top view of the channel. The connectors connect the canonical amino acid residues of the indicated binding sites. **B: Left** – the see-through side view of a RyR1 tetramer (Ca-inactivated state, rabbit 7tdg (Nayak and Samso, 2022)); top – the cytoplasmic side, bottom – the SR luminal side. **Right** - the detail of regions involved in the RyR operation. Colors correspond to A. Green spheres - Ca atoms at the activation binding sites, and at the ACP molecule bound at the ATP site (center). The brown color indicates the S23* loop of the neighbor monomer. The short red dotted lines correspond to the salt bridges between residues K4101-D4730* and E4075-R4736* (red arrows in A). G - the hinge and gate residues D4934 and I4937 of the S6 segment.

Another region that seems to play a role in divalent-ion-dependent inactivation is the S23 loop. Three amino acids (R4736, Y4733, G4732) of the S23 loop were proposed as important components of Ca^{2+}-dependent inhibition in rabbit RyR1 (Gomez et al., 2016). Their mutation induces malignant hyperthermia (MH) and increases the IC50 for calcium-dependent inhibition. Indicatively, the S23 loop was found nearer the EF-hand region of the adjacent monomer in the RyR1 structure obtained at 10 mM Ca^{2+} than in the structure at <0.1 µM Ca^{2+} (Efremov et al., 2015). The EF-hand region and the S23 loop of

173 a neighbor RyR monomer were connected by salt bridges in the inactivated RyR1 structure but the salt
174 bridges were not present in the open RyR1 structure determined under the same conditions (Nayak and
175 Samso, 2022). Since no Ca atom was resolved in the EF-hand region of either of the structures, these
176 authors proposed a kinetic mechanism of RyR1 inactivation that does not require further Ca^{2+} binding.
177 Specifically, they suggested that the activation of RyR1 by Ca^{2+} ions may lead, after a delay, to the
178 interaction between the EF-hand region of one monomer and the S23 loop of the other monomer. This
179 would thus result in the transition to the inactivated state locking the Ca^{2+} ion at the activation site and
180 prohibiting reactivation before removal of the inhibition (Nayak and Samso, 2022). This hypothesis,
181 however, does not comply with the steady-state open probability of RyR1 observed in single-channel
182 experiments (Chu et al., 1993; Laver et al., 1997) that showed a bell-shaped dependence on calcium
183 concentration and thus indicated the presence of two different binding sites – one for activation and
184 one for inhibition. Taking together the findings mentioned above, it may be concluded that the EF-hand
185 region is a serious candidate for the RyR inhibition site; however, a functional or structural explanation
186 of the differences between the RyR1 and RyR2 inhibition was not revealed. Part of the problem is in the
187 relatively low resolution of the EF-hand region in cryo-EM structural studies.

188 Another RyR region that was shown to participate in the regulation of RyR activity is the S45 linker
189 (amino acid residues 4820-4833 in rRyR1). Alanine substitution of residues T4825 or S4829 in RyR1
190 decreased its sensitivity to caffeine, the maximum of the open probability, and the maximum of
191 ryanodine binding, while the mutation L4827A and the MH-linked mutation T4825I increased both
192 maxima (Murayama et al., 2011). Moreover, the MH mutations T4825I and H4832Y were reported to
193 increase the IC50 of RyR1 to inactivation by Ca^{2+} (Gomez et al., 2016). Thus, this segment plays a role in
194 both the activation and the inactivation of the ryanodine receptor.

195 Most of the published RyR structures were collected under experimental conditions that vary between
196 laboratories. As a result, the electron density maps vary and deductions inferred from individual maps
197 and structural models may not be equally valid for particular aspects. Similar problems occurred with
198 recordings and interpretation of functional experiments. The question arises as to whether these are
199 even compatible. If yes, it should be possible to construct a functional model from structural data that
200 would explain functional data. To this aim, we selected a large set of published RyR1 and RyR2
201 structures determined under conditions comparable with relevant single-channel experiments and
202 estimated relationships between divalent ion binding and signaling pathways. We focused on the
203 allosteric mechanism of RyR control by divalent ions, with the use of bioinformatic and structural
204 analysis methods. We compare RyR1 and RyR2 structures and construct a fundamental allosteric
205 mechanism common for both RyR isoforms. The proposed mechanism is verified by an operational
206 model of the RyR channel open probability based on the MWC theory (Monod et al., 1965) and
207 statistical mechanics (Marzen et al., 2013).

208 ## Results

209 To correlate the structure of RyR with its function we took advantage of published RyR structures and
210 RyR open probabilities obtained under similar conditions. RyR structures selected for analysis were
211 obtained under conditions stabilizing the closed, primed, open, or inactivated structural states. RyR2
212 structures of the inactivated state have not been published yet. Open probabilities of both RyR1 and
213 RyR2 selected for analysis were determined at Ca^{2+} and Mg^{2+} concentrations causing activation and
214 inhibition of RyRs. All structures and open probabilities analyzed here are listed in Supplementary Table
215 S1.

216 Below we first examine the molecular structure of the EF-hand pair EF1/EF2, the candidate inhibition
217 site, for its propensity to bind divalent ions. Second, we analyze the spatial interaction between the EF-
218 hand region and the S23 loop, the proposed inactivation path. Third, we evaluate the relative positions
219 of the RyR central core domains relevant to the RyR single-channel activity regulation, in all examined
220 RyR states and isoforms. Fourth, we identify the allosteric network in both RyR isoforms from the
221 regulatory allosteric sites to the channel gate for the representative RyR states. Fifth, we construct a
222 comprehensive model of RyR operation and use it to calculate the dependences of RyR1 and RyR2 open
223 probabilities on the divalent ion concentration. Finally, we compare the model predictions with the
224 relevant single-channel open probability data.

225 ### 1 The propensity of EF1 and EF2 loops to bind divalent ions

226 In all RyR structures, EF1 and EF2 have a form of a typical EF-hand pair, similar to Ca-binding sites of
227 specialized Ca-binding proteins. To evaluate and compare their ability to bind divalent ions we used the
228 identity score (IS) of EF-hand loops (see Methods), which has a maximum value of 12/6/3 (21) for
229 calmodulin. The sequence of the EF1 loop in RyR1, VTDPRGLISKKD, the same in all examined mammals
230 (rabbit, rat, mouse, human, dog, and pig), has IS of 10/4/2 (16). The corresponding EF1 loop sequence
231 for RyR2 is DPDGKGIISKRD for the rabbit and DPDGKGVISKRD for the other examined mammals, both
232 having IS of 11/5/3 (18), by 2 points higher than for the EF1 of RyR1. The sequence of the EF2 loop is
233 EADENEMINCEE in human, mouse, and rat RyR1; EADENEMINFEE in rabbit RyR1, and EADENEMIDCEE in
234 pig RyR1, while in RyR2 it is ETDENETLDYEE in all examined species. All EF2 sequences have an IS of
235 10/5/2 (17). The identity score of the scrambled RyR1 EF1 sequence YDGDKPSKLDIT (Fessenden et al.,
236 2004) is 9/4/2 (15), that is, by 1 point lower than that of EF1 in WT RyR1. The scores of EF1 and EF2 are
237 comparable with the calmodulin EF-hand sequence score of 12/6/3 (21) suggesting that both the EF1
238 and EF2 loops and even the scrambled EF1 loop can bind divalent ions but probably with a reduced
239 affinity and selectivity.

240 We examined the theoretical ion binding ability of EF1 and EF2 hands in the region corresponding to
241 rRyR1 residues 4063-4196, which starts ahead of the EF-hand region and ends behind the U-motif onset,
242 to keep the secondary structure intact. This region was extracted from 10 recent RyR1 and RyR2
243 structures specified in Supplementary Table S1. The scrambled versions of EF1 were created using RyR
244 structures determined at high Ca^{2+} concentration (Nayak and Samso, 2022), in which the wild-type EF1
245 sequence of amino acids 4079-4092 was replaced by the scrambled sequence YDGDKPSKLDITRV
246 (Fessenden et al., 2004). Finally, all structures corresponding to rRyR1 residues 4063-4196 were

247 subjected to energy minimization and submitted to the MIB2 server for evaluation of the ion binding
248 score (IBS) of individual amino acid residues and the number of ion binding poses (NIBP) for Ca and Mg
249 ions. The IBSs were estimated for amino acid residues 1, 3, 5, 7, 9, and 12 of the EF1 and EF2 loops
250 involved in ion binding. As a comparison baseline, we used the residues of 4063-4196 without the 12
251 metal-binding residues. The number of IBPs was determined as the number of all poses that involved at
252 least 2 residues of the ion binding loops. Table 1 presents statistics on IBS and NIBP data.

253 The IBS values of the ion-binding residues of both EF1 and EF2 were significantly larger than the IBS
254 values of the remaining residues (KWANOVA, $p < 0.001$). ANOVA analysis indicated that IBS of EF1 for
255 Ca^{2+} ions was significantly higher in RyR1 and RyR2 than in the RyR1scr structures ($p = 0.0128$ and
256 $p < 0.001$) but for Mg^{2+} ions only the difference between RyR2 and RyRscr was significant ($p < 0.001$). EF1
257 and EF2 bind Ca^{2+} equally in both isoforms. In RyR2, EF2 binds Mg^{2+} more strongly than EF1 ($p = 0.0028$)
258 while in RyR1 both EF hands bind Mg^{2+} equally. Importantly, however, the EF1 had an IBS for Ca^{2+} and
259 Mg^{2+} significantly larger in RyR2 than in RyR1 ($p = 0.0011$ and 0.0014, respectively). The extent of these
260 differences can be assessed by comparison with calmodulin (Table 1), which also possesses two pairs of
261 EF-hands that bind M^{2+}, albeit with micromolar affinity. The lower IBS values of EF-hands in RyRs are
262 consistent with the observed sub-millimolar concentration range of inhibitory potency of Ca^{2+} and Mg^{2+}
263 in RyR isoforms.

264 **Table 1. The ion-binding ability of EF1 and EF2 in RyR isoforms.**

Structure	N	IBS (mean ± SEM)						NIBP (mean ± SEM)			
		EF1		EF2		Baseline		EF1		EF2	
		Ca	Mg	Ca	Mg	Ca	Mg	Ca	Mg	Ca	Mg
RyR1	10	0.7±0.1	0.4±0.1	0.8±0.2	0.8±0.1	-0.07±0.03	-0.06±0.03	1.9±0.4	0.7±0.3	4.3±1.4	2.4±0.8
RyR2	10	1.2±0.1	1.1±0.1	1.5±0.2	1.7±0.1	-0.14±0.03	-0.13±0.03	6.6±1.8	2.1±0.4	9.3±2.3	5.1±1.4
RyR1scr	7	0.2±0.1	0.2±0.1	0.7±0.1	0.7±0.1	-0.04±0.03	-0.04±0.03	0.7±0.4	0.9±0.3	2.1±0.7	1.7±0.6
CaM-N	1	2.3	2.2	2.3	2.2	-0.42	-0.41	56	8	42	5
CaM-C	1	1.6	2.0	1.8	1.8	-0.37	-0.39	8	4	37	7

265 IBS - ion binding score. NIBP - ion binding poses. N – the number of evaluated RyR structures. RyR1scr stays for the
266 RyR1 with scrambled EF1-hand sequence. CaM-N and CaM-C stay for the N-terminal and C-terminal EF-hand pairs
267 of calmodulin, respectively. The values for calmodulin were estimated using the structure 1exr (Wilson and
268 Brunger, 2000).

269 The estimates of NIBPs (Table 1) emphasize findings on IBS of the RyR1 and RyR2 EF-hands, regarding
270 their sensitivity to the type of divalent ion. As demonstrated, the NIBP of CaM-N and CaM-C for Ca^{2+} is
271 markedly higher than that for Mg^{2+}, in agreement with the known selectivity of calmodulin for these
272 ions. In both EF1 and EF2 of RyRs, the difference in NIBP of Ca^{2+} and Mg^{2+} is small, indicating low
273 selectivity for divalent ions. Comparison of NIBP in RyR isoforms indicates a better binding of M^{2+} in
274 RyR2 than in RyR1. The structures with scrambled EF1 loop returned lower values of IBS and NIBP.

275 The lower IS, IBS, and NIBP values of the scrambled RyR1 structures are in agreement with the
276 decreased Ca^{2+} inhibitory potency of the scrambled EF1-hand RyR1 construct (Fessenden et al., 2004).
277 The higher IBS and NIBP for Ca^{2+} and Mg^{2+} of the EF1-hand in RyR2 than in RyR1 is at odds with the
278 weaker inhibition of ^{3}H-ryanodine binding by Ca^{2+} ions in RyR1 channels with their EF1 motif exchanged
279 for the RyR2 counterpart (Gomez and Yamaguchi, 2014), suggesting that the effect of this exchange
280 cannot be caused by the higher Ca^{2+} affinity of the EF1 loop in RyR1 than in RyR2.

281 The EF2 of RyR2 has the same IS but somewhat higher IBS and NIBP values than the EF2 of RyR1. This
282 theoretical result is in line with the lack of the effect of the exchange of the RyR1 region around the EF2
283 for the corresponding RyR2 region on the Ca^{2+}-dependent inhibition of ryanodine binding (Gomez and
284 Yamaguchi, 2014), meaning that the difference between Ca-dependent inactivation of RyR1 and RyR2 is
285 not caused by the properties of the EF2 hand.

286 To summarize, the theoretical ion binding results provided no support for the hypothesis that the
287 difference between RyR isoforms comes from the different affinity of their putative inhibitory sites to
288 divalent ions. On the contrary, they indicate a substantial ability of EF1 and EF2 to bind divalent ions, a
289 prerequisite to constitute the inhibitory Ca-binding site.

290 2 Spatial interactions between the EF-hand and S23* regions

291 As we reasoned above, the difference in the propensity of the EF-hand region to bind divalent ions
292 cannot explain the difference in the Ca-dependent inactivation between RyR isoforms. The question is
293 then whether the difference can reside in the transmission of the ion-binding signal from the EF-hands
294 to the channel gates. A clue was provided by Gomez et al. (2016) who found that malignant
295 hyperthermia mutations of three amino acids of the S23 loop shifted the inhibition of ryanodine binding
296 in RyR1 to a higher Ca^{2+} concentration, close to that of the RyR2, and proposed that these three amino
297 acids are involved in the inter-monomeric interaction of the S23* loop with the EF-hand region (Gomez
298 et al., 2016). Nayak and Samsó (Nayak and Samso, 2022) measured the distance between the EF-hand
299 region and the S23* loop as the distance between pairs of residues allowing direct interaction at
300 sufficient proximity. These included glutamate E4075 to arginine R4736* (distance D1) and lysine K4101
301 to aspartate D4730* (distance D2) in rabbit RyR1 structures. Both distances showed a tendency to
302 decrease among RyR1 structures in the order closed (7k0t) > open (7tdh) > primed (5taq) ≈ Ca-
303 inactivated (7tdg), indicating that these two pairs of residues may play a role in RyR1 inhibition (Nayak
304 and Samso, 2022). We measured both distances in the whole set of RyR structures to examine the
305 difference between the RyR isoforms.

306 The D1 distances measured between Cα atoms of the E4075-R4736* pair are summarized in Figure 2,
307 and compared with the theoretical estimate of the maximal distance allowing their interaction. The
308 median of D1 values measured in the RyR1-C structures is too large for the residues to interact, while
309 those of the open, primed, or inactivated RyR1 structures are in the range allowing for proper
310 interaction between residues in a suitable rotamer configuration. Of interest is the RyR1-Mg structure
311 7umz, defined as "ACP/10mM free Mg^{2+}-closed state" (Nayak et al., 2024), obtained at a very high
312 concentration of Mg^{2+} ions that are supposed to stabilize the inactivated state (Laver et al., 1997). This
313 structure provided D1 similar to those found in primed, open, and inactivated states. The D1
314 measurements in RyR2 structures provided completely different results. In all RyR2 states the median
315 D1 is substantially larger than that in RyR1 and, importantly, also larger than the maximum interaction
316 distance estimated for hRyR2 D4030-R4665* (the equivalent of rRyR1 E4075-R4736*).

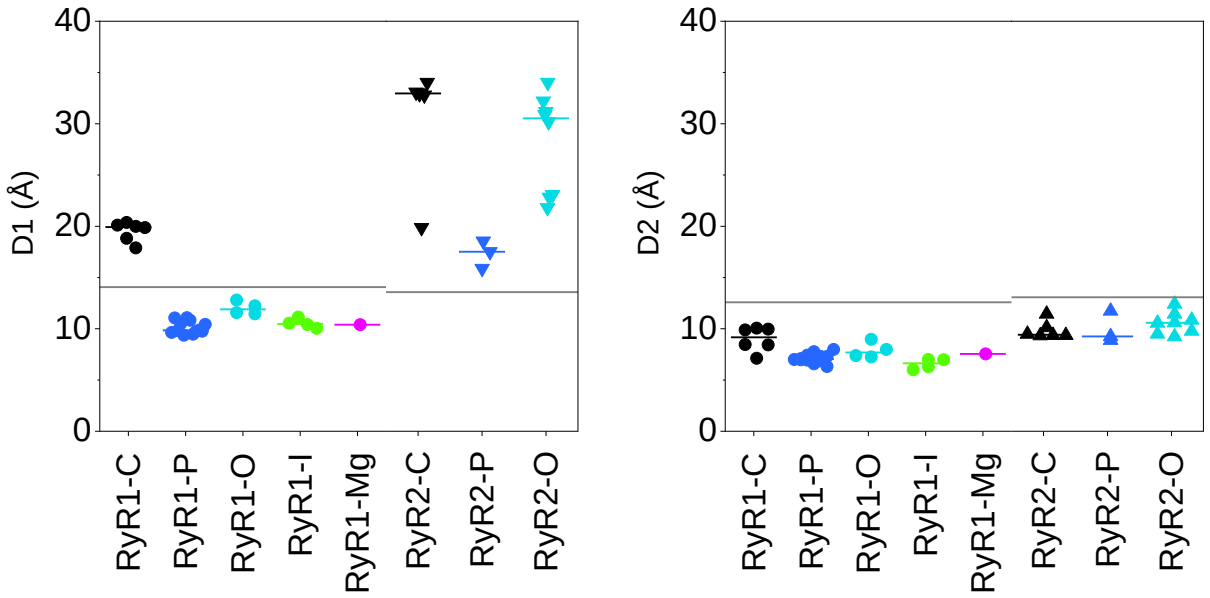

Figure 2. **Distances between key amino acid pairs of the EF-hand and S23* in RyR structures. Left** – Distances D1 between E4075 – R4736* or equivalent. **Right** - Distances D2 between K4101 – D4730* or equivalent. Circles - RyR1 states. Triangles - RyR2 states. C – closed state, black symbols. P – primed state, blue symbols. O – open state, cyan symbols. I – inactivated state, green symbols. Mg – high-magnesium state, magenta symbols. Short lines - the median values of groups. Long lines – the theoretical maximum distances allowing H-bond formation.

317 Measurements of D2 distances yielded only subtle distinctions between RyR structures (Figure 2, right).
318 In all RyR1 structures, the median D2 values were neither substantially nor statistically different. In all
319 RyR1 states, the K4101-D4730* separation allowed for proper residue interaction by H-bonds. In RyR2
320 structures, the D2 medians of individual states were only slightly larger than those in the respective
321 RyR1 structures, much less so than in the case of D1 distances. The D2 medians of closed, open, and
322 primed RyR2 states were similar and in the theoretical H-bond interaction range.

323 These results indicate that the glutamate-arginine* (E4075 and R4736*) distance D1 between the EF-
324 hand and S23* regions is too large in all RyR2 structures, in contrast to the RyR1 non-closed states
325 including the inactivated state, in which the residues may potentially interact and transmit the binding
326 signal. On the other hand, the D2 distances in all RyR1 and RyR2 structures assume values that may
327 allow interaction of the lysine with the aspartate* (K4101-D4730*) in RyR1 or with the glutamate* in
328 RyR2, and thus potentially participate in signal transmission.

329 The resolution of published cryo-EM RyR structures is typically about 3-4 Å, which limits conclusions
330 based only on estimates of specific interaction distances. Moreover, we cannot exclude the presence of
331 interactions among other residues. A more robust measure of domain interactions could be the contact
332 area between the juxtaposed surfaces of the EF-hand region and the S23* loop, and the number of
333 possible electrostatic interactions (H-bonds and salt bridges) between their residues on the same set of
334 RyR1 and RyR2 structures. For this purpose, the motifs corresponding to rabbit RyR1 residues E4032 –
335 E4182 of one monomer, and to rabbit RyR1 residues D4695 - L4745 of the neighboring counterclockwise
336 monomer were cut out from the corresponding RyR structures, optimized, and submitted to the
337 PDBePISA server (see Methods for details). The results, summarized for all analyzed structures in Figure
338 3, point to a substantially larger contact area and number of interactions in primed, open, and

inactivated RyR1 structures than in closed RyR1 and closed, primed, and open RyR2 structures, in line with the distance measurements presented above. The RyR1-Mg structure 7umz (Nayak et al., 2024), provided both values similar to those found in primed, open, and inactivated states. The contact area and the number of electrostatic interactions correlate more steeply in RyR1 than in RyR2 structures. This indicates that the spatial arrangement of the two domains in RyR2 structures does not support the formation of electrostatic interactions as efficiently as in RyR1 structures, even if the two domains are near each other.

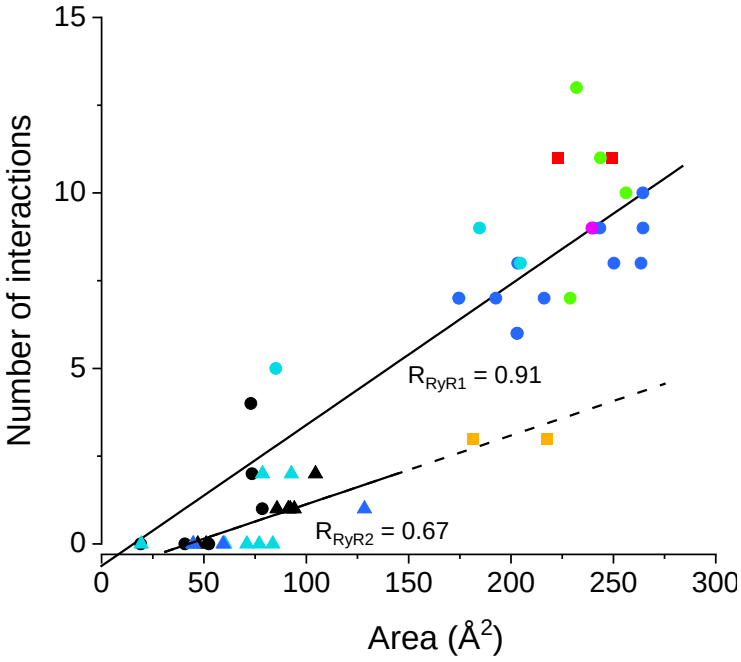

Figure 3. Number of interactions and area between the EF-hand region and S23* loop in RyR structures. Circles - RyR1 structures; Triangles - RyR2 structures; Black - closed state; Blue – primed state; Cyan – open state; Green - inactivated state; Magenta – high-Mg state. Orange squares - inactivated RyR1 with MH mutations R4736W, R4736Q; Red squares - inactivated RyR1 with MH mutations G4733E, F4732D. R_{RyR1}, R_{RyR2} - Pearson's correlation coefficients for RyR1 and RyR2 data groups (solid lines); n_{RyR1} = 27; n_{RyR2} = 17; $p < 0.005$ in both cases). Note: the correlations were calculated without the data for mutated structures (squares). The dashed line extrapolates the correlation line.

After optimization, 24 out of 27 RyR1 structures formed H-bonds and/or salt bridges between at least one of the residue pairs Q4100-I4731*, (E4075/D4079)-R4736*, (Q4100/K4101)-D4730* in all RyR1 states. The maximum number of simultaneous hydrogen bonds detected by the PDBePISA server was 6. On the other hand, in the corresponding RyR2 structures only 8 out of the 17 analyzed structures formed interactions between EF-hand - S23* residue pairs, with a maximum of two hydrogen bonds in a single structure. Moreover, the EF-hand aspartate and glutamate (corresponding to E4075 and D4079 in RyR1) could not form contact with the arginine corresponding to rRyR1 R4736*, the key S23* residue, in any RyR2 structure. These data suggest that interactions between the basic arginine residue R4736* and the acidic residues at the start of the initial helix E of the EF1-hand are specific for Ca^{2+}-dependent inactivation in RyR1, whereas the interactions between the lysine K4101 that immediately follows the F helix of EF1 and the middle of the S23* loop (corresponding to D4730* and I4731* in RyR1) may play a part in the inactivation of both RyR1 and RyR2 isoforms.

Interestingly, the replacement of arginine R4736* for tryptophan or glutamine in RyR1 that alleviates RyR1 inhibition by Ca^{2+} (Gomez et al., 2016) provided a reduced number of interactions per interaction area (Figure 3, orange squares), similar to that predicted for RyR2 type interaction. However, replacements of glycine G4733* for glutamate and phenylalanine F4732* for aspartate, also known to alleviate RyR1 inhibition by Ca^{2+} (Gomez et al., 2016) did not affect the number of interactions (Figure 3,

363 red squares). This means that the electron donor residue arginine R4736* is probably important for the
364 transmission of the divalent ion binding signal from the EF-hands to the S23* loop in RyR1. On the other
365 hand, the mutations G4733E and F4732D, both introducing a negative charge on S23, may act by
366 neutralizing the positive charge of R4736 thus making the transmission less effective without changing
367 the number of possible interactions.

368 3 Relative positions of the RyR core domains

369 The above distance analyses suggested clearly that the relative positions of the EF-hand and S23* loop
370 are state- and isoform-specific, and thus may affect the propensity of RyR1 and RyR2 for M^{2+}-dependent
371 inactivation. Additional contributions to the inactivation could arise from other domains involved in the
372 signal transmission that may assume different relative positions and shapes in specific RyR states and
373 isoforms. Previous RMSD (root mean square displacement) analysis of the backbone Cα atoms revealed
374 that the position of the C-terminal domain relative to the Central domain was shifted in primed and
375 open RyR1/RyR2 structures from the position in closed structures (Miotto et al., 2022; Nayak and
376 Samso, 2022). An even higher degree of the C-terminal domain shift was present in the inactivated RyR1
377 structure 7tdg (Nayak and Samso, 2022).

378 We inspected differences in conformational states of core domains located along the C-terminal quarter
379 of the RyR monomer by means of the RMSD analysis using the same set of RyR structures as analyzed
380 above. To begin with, the analyzed RyR structure and the reference RyR structure were aligned by their
381 Central domains, selected as the aligning reference for sufficient size and well-defined state-
382 independent structure. The distances between the corresponding Cα atoms of domains of interest in the
383 tested and the reference structures were then used to calculate their $RMSD_{100}$ values. The graphs of
384 Figure 4 compare $RMSD_{100}$ estimated relative to the closed RyR1 structure 7k0t (horizontal axis) and the
385 inactivated RyR1 structure 7tdg (vertical axis). The S45 linker, known to participate in RyR gating, could
386 not be analyzed in this way since its length of 13 residues is insufficient for correct $RMSD_{100}$
387 determination (Carugo and Pongor, 2001). The $RMSD_{100}$ of domains in the same state and isoform were
388 nearly always spread within a circle with a radius of 1 Å for all RyR structures. Thus, we considered the
389 structure of a RyR region to differ between channel states if their mean $RMSD_{100}$ values differed by more
390 than 2 Å (Carugo and Pongor, 2001).

391 Comparison of domain positions in RyR1 and RyR2 structures

392 The $RMSD_{100}$ values of the Central domain in all RyR structures were similar and independent of the RyR
393 state or isoform (Figure 4 A), as required for the self-aligned reference domain.

394 The C-terminal domain and U-motif (Figure 4 B and C) of all RyR1-C and RyR2-C structures (black
395 symbols) showed similar $RMSD_{100}$ values close to those of the reference closed structure (7k0t). The
396 RyR1-I structure 7umz, obtained in the presence of high Mg^{2+} concentration, showed $RMSD_{100}$ values
397 halfway between those of closed and inactivated RyR1 structures.

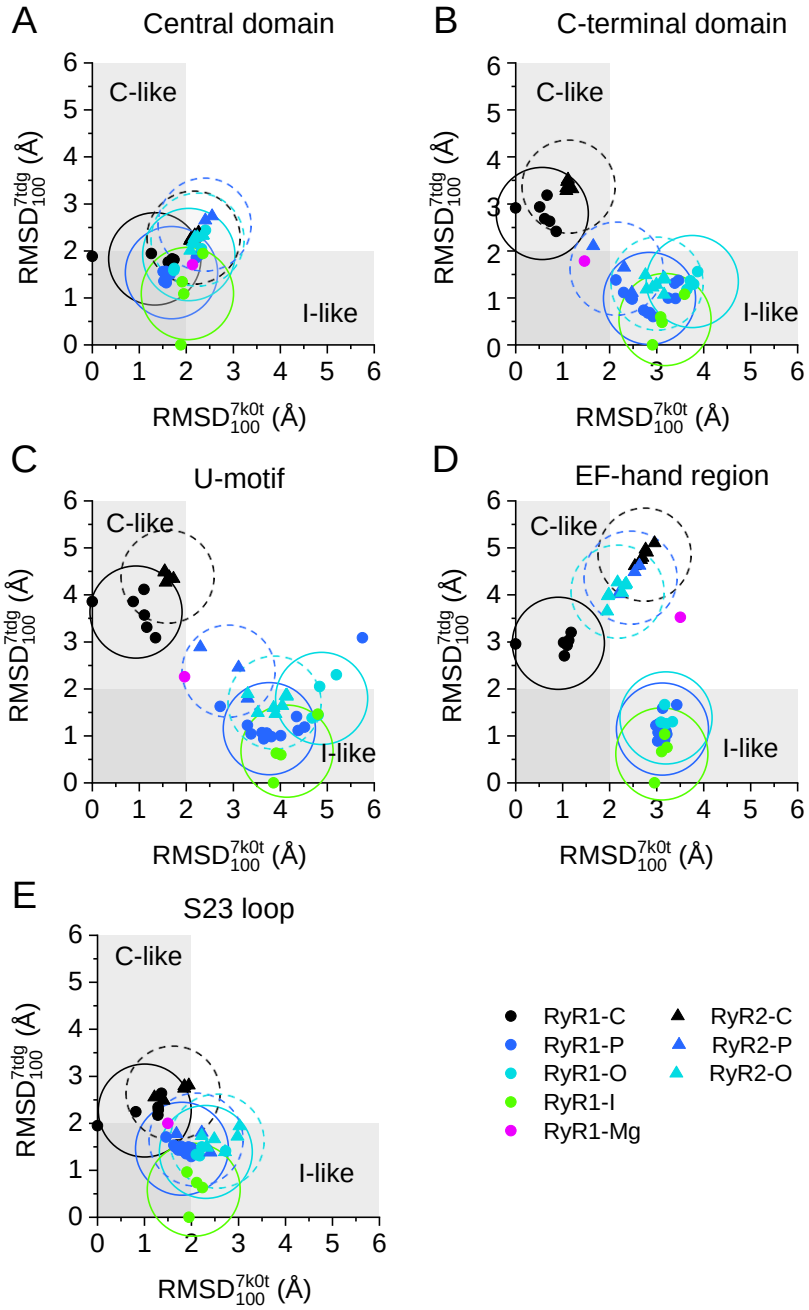

Figure 4. The RMSD analysis of RyR structures. Horizontal axis - $RMSD_{100}$ of the RyR structures relative to the closed RyR1 structure 7k0t. Vertical axis - $RMSD_{100}$ of the RyR structures relative to the inactivated RyR1 structure 7tdg. The circles of 1 Å radius are centered on the mean RMSDs of the corresponding group of RyR isoforms and states and appraise the significance of differences between groups (when the corresponding circles do not intersect the difference is significant). The solid circle data points and the solid circle lines indicate RyR1 data; The solid triangle data points and the dashed circle lines indicate RyR2 data. Colors indicate RyR states (see inset). C-like and I-like grey bands indicate the similarity of $RMSD_{100}$ values to either the closed or inactivated reference states.

In almost all other RyR1 and RyR2 structures, RMSDs of these domains were similar and close to that of the reference inactivated structure (7tdg). This confirms the displacement of the CTD and U-motif relative to the Central domain in primed, open, and inactivated RyR1 structures, observed previously by Nayak and Samso (Nayak and Samso, 2022) for the open 7tdh, primed 7tdj, and inactivated 5taq RyR1 structures. Moreover, it reveals qualitatively and quantitatively similar rearrangements from the closed to the primed or open states in both the RyR1 and RyR2 isoforms, indicating their similar responsiveness to the activation and inactivation conditions in both RyR isoforms.

The EF-hand domains of RyR1 and RyR2 structures displayed markedly dissimilar RMSDs. In RyR1, the open, primed, and inactivated structures (colored circles) were notably different from the closed but very close to the inactivated reference (RyR1) structure. The structure 7umz, obtained at a high Mg^{2+}

408 concentration, showed $RMSD_{100}$ values significantly different from both the closed and inactivated
409 reference RyR1 structures. In RyR2, the EF-hand region of all structures (triangles) also displayed notably
410 different $RMSD_{100}$ values relative to either of the reference (RyR1) structures (Figure 4 D). These data
411 reinforce the evidence of the structural differences between the EF-hands of RyR1 and RyR2 isoforms
412 indicated by the distance analysis above.

413 The RMSD values of the S23 loop in all RyR structures were low, almost the same, and similar to those of
414 both the closed and inactivated reference structures. This points to the very high structural stability of
415 the S23 loop within the RyR monomer relative to the Central domain.

416 Comparison of domain positions in different RyR states

417 In all domains except the EF-hand, the RMSDs of the closed RyR1 and RyR2 structures were very similar
418 irrespective of the isoform. The RMSDs of the primed, open, and inactivated RyR1 structures and the
419 open and primed RyR2 structures were also very similar but markedly different from those of the closed
420 RyR1 and RyR2 structures. However, while there is a pronounced difference between the mean $RMSD_{100}$
421 of the EF-hand in closed RyR1 structures on the one hand and the open, primed, and inactivated RyR1
422 structures, the differences between the closed, open, and primed RyR2 structures are not significant.
423 This pronounced distinction in the EF-hand position between RyR1 and RyR2 indicates that the
424 inactivation signal in RyR2 may have a lower chance of passing to the neighbor monomer. These findings
425 also indicate that in RyR1 channels, the structural prerequisites for the inactivation signaling are present
426 also in primed and open channels and that the binding of divalent ions to the inhibition site at the EF-
427 hand region may constitute the inactivation signal.

428 Whereas the relative positions of all five examined domains were similar in the primed, open, and
429 inactivated states (Figure 4), these states differed by their flexion angle (see Methods). Despite the large
430 dispersion, the medians of flexion angles showed a tendency to decrease in both RyR1 or RyR2
431 structures in the order: closed state ≥ primed state ≥ high Mg^{2+} state ≥ open state ≥ inactivated state, in
432 RyR1; closed state ≥ primed state ≥ open state, in RyR2 (see Supplementary Table S1 for details).

433 Interaction of EF-hand region with S23 loop.

434 To better understand the above-disclosed difference in the displacement of the EF-hand region and S23
435 loop between RyR1 and RyR2 structures (Figure 4 D and E), we aligned the RyR1-O and RyR2-O model
436 structures on their more static S23* loop (Figure 5). We compared here only the open states, since
437 according to the distance analysis (Figure 2) the distances in the closed states are too large, the
438 inactivated RyR2 structure is not available, and the distances D1 and D2 are similar in RyR1-O and RyR1-
439 I. A close look at the structure of the EF-hand region (Figure 5 A) reveals substantially different
440 conformations of the two isoforms in the segment starting just before EF1 and ending just after EF2
441 (residues 4052-4140 in rRyR1). In RyR2, both EF1 and EF2 are diverted downward relative to their
442 counterparts in RyR1. As a consequence, the D4030 of RyR2 (the equivalent of E4075 in RyR1) withdraws
443 from its interaction with S23* (Figure 5 B, C). This confirms the results of the distance analysis, namely
444 that RyR1 structures can make hydrogen bonds between E4075 and R4736* and between K4101 and
445 D4730*, while the corresponding RyR2 structures can make a hydrogen bond only between K4056 and

E4659* but not between D4030 and R4665* (hRyR2 numbering). The difference stems most probably from the low sequence identity (52%) for the EF-hand region (rRyR1 4071-4137 and hRyR2 4026-4092). This is much less than the sequence identity of the adjacent U-motif (81%) and the Central domain (82%), at which RyR1 and RyR2 are aligned much better (Figure 5 A).

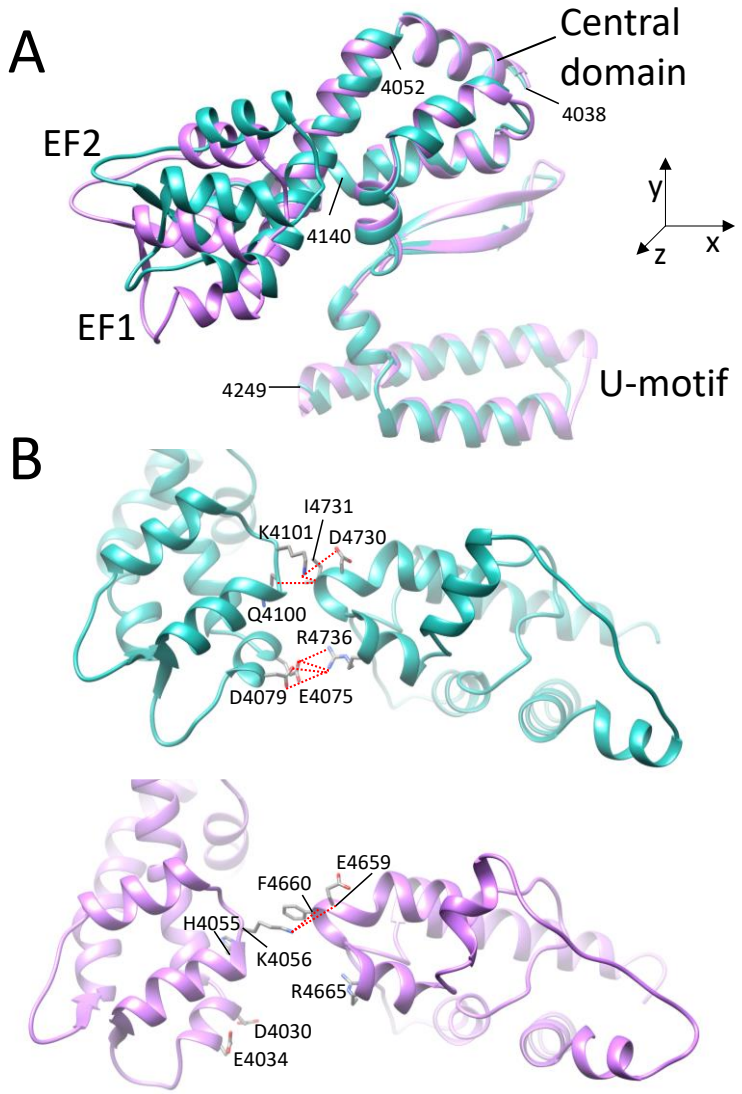

Figure 5. Structural interactions between the EF-hand and S23 in the open RyR1 and RyR2 structures. **A** – Overlay of the EF-hand region in the RyR1-O (7m6l, cyan) and RyR2-O (7ua9, magenta) structures aligned at their S23 loops (out of the image plane). Note the differences in the EF1 and EF2 positions and almost the same positions of the Central domain and U-motif segments. The RyR1 residue sequence numbers are given for orientation. **B** – Residue interactions between the EF-hand region (left) and S23* loop (right) in the RyR1-O (cyan) and RyR2-O (magenta) structures. The structures in B are rotated by 30° counterclockwise about their x, y, and z axes relative to their orientation in A. Dotted red lines -– structurally possible H-bonds between the interacting residues.

4 Allosteric pathways from the ion-binding sites to the gate.

Transmission of a signal from the regulatory site to the active site should proceed by propagation of a perturbation through a sequence of contacts between nearby residues. This principle is used in the OHM server for the detection of allosteric pathways (Wang et al., 2020). Previously, analysis of such pathways in RyR1 structures revealed how the cytosolic calcium, ATP, and caffeine activate RyR1 (Chirasani et al., 2022). Here we have used the OHM server to explore the regulatory network of both ion-dependent allosteric pathways. We will use the term “activation pathway” for the pathway commencing at the high-affinity Ca^{2+}-binding site, and “inhibition pathway” for the pathway commencing at the low-affinity,

458 low-selectivity M^{2+}-binding site associated with the inhibition site. Both will be considered in the model
459 of RyR operation.

460 Since the allosteric analysis requires a complete and correct structural model, only RyR structures with
461 the best resolution and the fewest missing residues were processed (see Methods). According to these
462 criteria we selected five RyR1 model structures: one closed (7k0t), one primed (7tzc), two open (7m6l
463 and 7tdh), and one inactivated (7tdg); and four RyR2 model structures: two closed (7vmm and 7ua5)
464 and two open (7vmp and 7ua9). The structures 7tdg and 7tdh represent two RyR1 state configurations
465 in the same sample; similarly, the structures 7ua5 and 7ua9 represent two RyR2 state configurations in
466 the same sample (see Supplementary_Data.zip for the sequences and structures of the models).

467 In the selected structures, we identified residues with high allosteric coupling intensities (ACI) for both
468 the inhibition and activation network and compared them with residues important for ligand binding
469 and gating of RyR (Table 2). These residues were then identified in individual paths and the paths
470 containing identical high-ACI residues were grouped. To increase the visibility of the main pathways,
471 residues with ACI less than 5% of the maximum ACI for the given structure were not considered. For
472 each RyR structure, this process precipitated in major pathways that shared residues of the regulatory
473 ligand-binding sites, inter-monomeric interaction sites, and the regulatory site of the S45 linker (Table
474 2).

475 Table 2. **The list of important residues examined for contribution to allosteric networks.**

Ligand binding sites	**Residue numbers (rabbit RyR1 numbering)** [#]
ATP binding site	**4211, 4214, 4215,** 4218, **4954, 4955**, 4957, **4958, 4959,** 4960, 4975, **4979**, 4983, **4984, 4985**
Caffeine binding site	**3753**, **4239**, 4242, 4671, **4715**, **4996**, 5011, **5014**, 5015
Interaction sites	
EF-hand region	4075, 4079, 4100, 4101
S23* loop	4730*, 4731*, 4736*
Regulatory site	
S45 linker	4821-4834

476 [#] Residue numbers in bold were originally defined as the ATP and CFF binding site-forming
477 residues by (des Georges et al., 2016).
478 The ATP and CFF binding sites were defined as a group of residues that formed contact
479 with a ligand in at least one of the RyR structures listed in Supplementary Table S1, given
480 that the position of a ligand in the structure is not well-defined (des Georges et al., 2016)
481 and that not all examined model structures contained a ligand at the binding site. The
482 interacting residues of the EF-hand– S23* regions were those identified by the PDBePISA
483 to form a salt bridge or an H-bond between neighboring monomers in at least one RyR
484 structure (Supplementary Table S1).

485 ## The inhibition network

486 In the inhibition network analysis, we defined the ion-binding loops of the EF1 and EF2 as the allosteric
487 inhibition site (INH), and the hinge and gate of S6 and S6* as the active site (GATE). In the network

488 output list of the OHM server (see Supplementary_Data.zip), large ACI values were observed at the ATP-
489 binding residues of the U-motif and the C-terminal domain, in addition to residues next to the EF-hand
490 loops and the GATE (Figure 6). In several model structures, ACIs larger than the threshold value also
491 occurred at several residues of the S45, S45*, and S23*segments.

492 Two major pathways denoted as the intra-monomeric and the inter-monomeric pathway were
493 identified in the structural models of both RyR isoforms. Both pathways displayed several branches that
494 partially fluctuated among model structures. Notably, most branches comprised residues either of the
495 ATP binding site, known to support the calcium-dependent activation (des Georges et al., 2016;
496 Chirasani et al., 2022), or of the S45 linker, known to participate in the regulation of channel gating
497 (Murayama et al., 2011; Gomez et al., 2016).

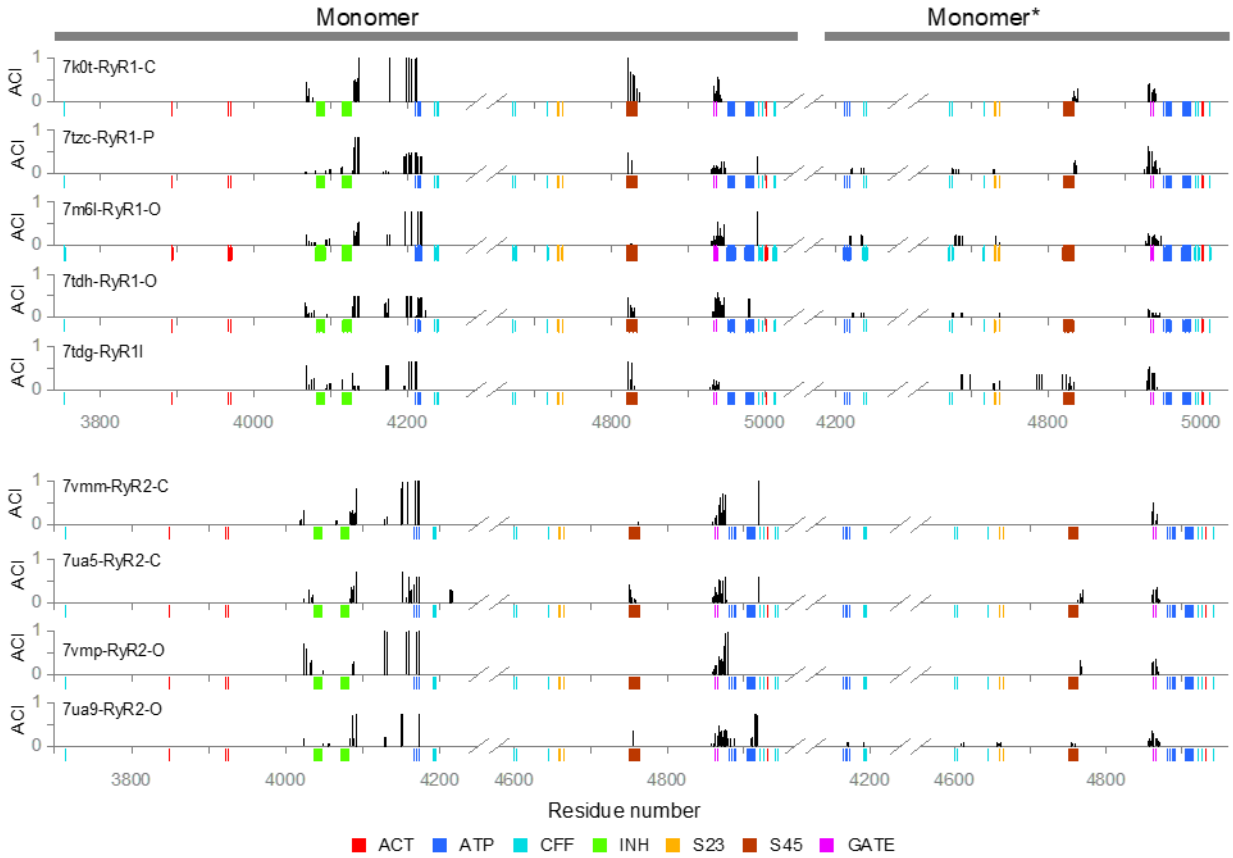

Figure 6. The allosteric coupling intensities of inhibition pathways. The ACIs were calculated for all detected inactivation paths and mapped on the RyR sequences. The graph displays only ACI > 0.05. The color-coded marks under the sequence axis indicate the positions of important residues from Table 2 and Table 8, see the legend at the bottom, where: ACT – Ca^{2+}-binding activation site, INH – M^{2+}-binding inhibition site, ATP – ATP-binding site, CFF – caffeine/xanthine binding site, S23 – S23 loop, S45 – S45 linker, and GATE – channel gating residues.

498 <u>The intra-monomeric inhibition pathway</u> was identified in all 9 investigated model structures and
499 represented 48 – 100 % of the first 100 inactivation paths generated by OHM for individual model
500 structures (see Supplementary_Data.zip). In both RyR isoforms, this pathway was formed by six major
501 branches (I1 – I6, Table 3; Supplementary Table S2) all passing through the U-motif and the ATP-binding

site residues. Each RyR model structure contained at least one but up to three intra-monomeric branches. Individual branches, which occurred in various proportions in different model structures, differed in specific residues of the ATP-binding site. Branches I4 – I6 also contained residues of the S45 linker, more often in RyR1 than RyR2 isoforms, and more often in the closed pore structures (C, P, I) than in the open structures. Individual structures contained 1 – 3 intra-monomeric branches. Three RyR1 and two RyR2 structures contained only 1 intra-monomeric branch.

Table 3. Fractional occurrence of branches in the inhibition network pathways.

Main branches connecting the INH and GATE sites		Fraction of paths (%)								
		RyR1					RyR2			
		C	P	O	O†	I†	C	C†	O†	O
		7k0t	7tzc	7m6l	7tdh	7tdg	7vmm	7ua5	7ua9	7vmp
Name	Intra-monomeric pathways									
I1	-EF - U - ATP - S6-		42	72	60		100	63		100
I2	-EF - U - ATP - S6-								18	
I3	-EF - U - ATP - S6-								74	
I4	-EF - U - ATP - S45 - S6-		53			48		24		
I5	-EF - U - ATP - S45 - S6-				27					
I6	-EF - U - ATP - S45 - S6-	100			4					
	Subtotal	100	95	72	91	48	100	88#	92	100
	Inter-monomeric pathways									
I7	-EF - S23* - U* - S6*-			14	9					
I8	-EF - S23* - U* - S6*-			14						
I9	-EF - S23* - U* - S6*-		5							
I10	-EF - S23* - U* - S45* - S6*-								8	
I11	-EF- S23*- S45*-S6*-					40				
I12	-EF- S23*- S45*-S6*-					12				
	Subtotal	0	5	28	9	52	0	0	8	0
	TOTAL	100	100	100	100	100	100	88#	100	100

INH and GATE are defined in Table 8. The abbreviations EF, U, ATP, S23, S45, and S6 refer to the EF-hand region, U-motif, ATP-binding site, S23 loop, S45 linker, and S6 helix, respectively. These domains contribute by one or more residues to the path (see Supplementary Table S2 for the list of critical residues of individual branches).

† marks a pair of RyR1 and RyR2 structures obtained in the same experiment. # The remaining 12% of the allosteric signal passed through the poorly resolved DR1 region.

<u>The inter-monomeric pathway</u> connecting the EF1/2 loops with the S23* loop was detected by OHM in 5 – 52 % of the first 100 inhibition paths for individual model structures (Table 3, Supplementary Table S2). This pathway diverged to 6 branches (I7 – I12), which all involved one of the S23* residues R4736*, D4730*, and I4731* or its hRyR2 equivalent F4660*, identical to those forming a salt bridge or H-bond with the EF-hand region as identified by the PDBePISA data (see above). Notably, this pathway was present in all RyR1 structures except for the RyR1-C but only in one RyR2 structure (Table 3). Individual RyR structures contained 1 – 2 inter-monomeric branches. In the primed and open RyR1 structures, this pathway participated by only 5 – 28 %, but it was dominant by 52% in the inactivated RyR1 structure

523 7tdg. In the RyR2 open structure 7ua9 it participated by 8% (branch I10). Notably, four out of 6 inter-
524 monomeric branches used the U*-motif: three in RyR1 and one in RyR2 structures. Two branches of the
525 inactivated RyR1 structure 7tdg connected the S23* with the S45* linker directly and not through the
526 U*-motif. The inter-monomeric pathway reached the gate *via* the S6* segment.

527 ## The activation network

528 In the activation network, we defined the Ca^{2+} binding residues of the CD and CTD as the allosteric
529 activation site (ACT), and the hinge and gate residues of the S6 and S6* as the active site (GATE). The
530 active site was the same as defined for the inhibition pathway analysis since no other gates are present
531 in the RyR pore. The large ACI values were observed at the ATP-binding site and the C-terminal domain
532 residues near the CFF binding site, in addition to residues contacting ACT and the GATE (Figure 7). In
533 several model structures, ACIs larger than the threshold value also occurred at several residues of the
534 S45 linker.

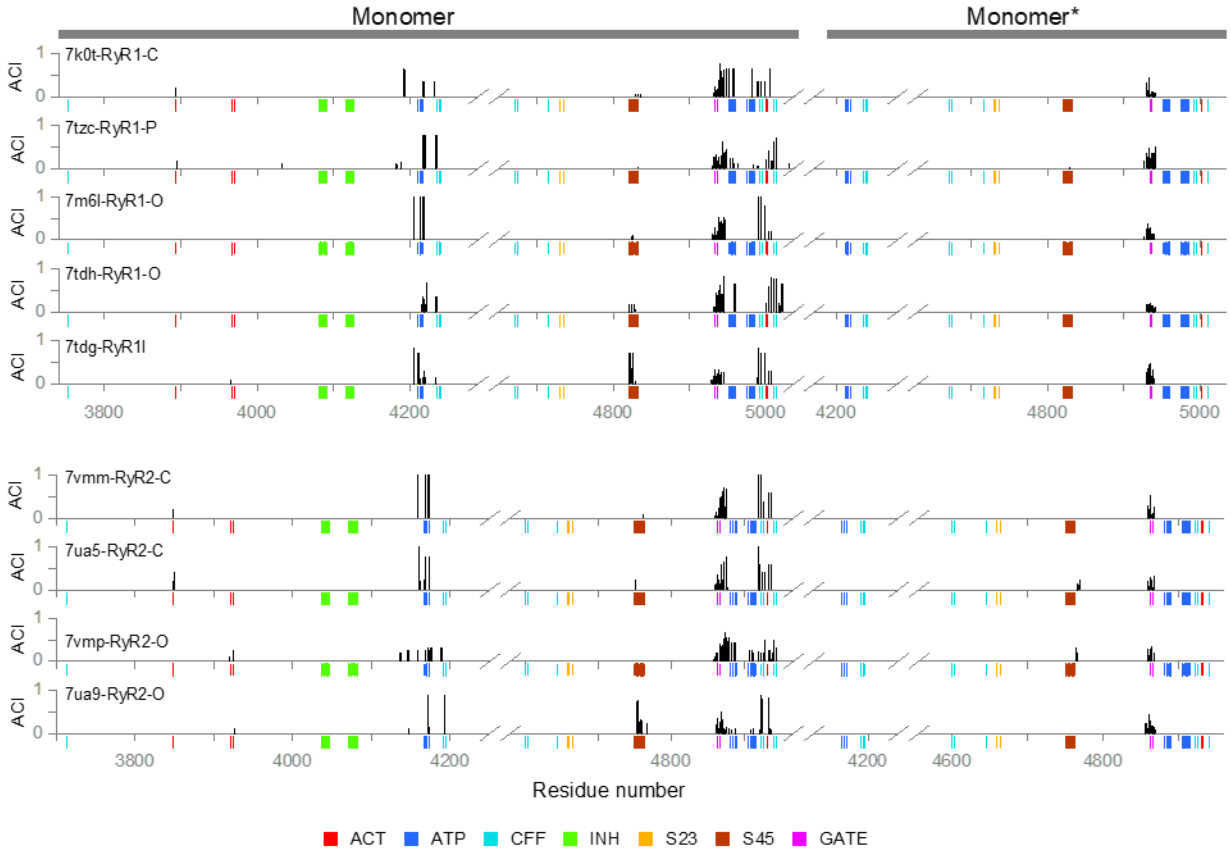

Figure 7. The allosteric coupling intensities of activation pathways. The ACIs were calculated for all detected activation paths and mapped on the RyR sequences. The graph displays only ACI > 0.05. The color-coded marks under the sequence axis indicate the positions of important residues from Table 2 and Table 8, see the legend at the bottom: ACT – Ca^{2+}-binding activation site, INH – M^{2+}-binding inhibition site. ATP – ATP-binding site, CFF – caffeine/xanthine binding site, S23 – S23 loop, S45 – S45 linker, GATE – channel gating residues.

535 The activation network consisted of a single intra-monomeric pathway with nine branches running close
536 to each other (Table 4; Supplementary Table S3). All branches comprised the CTD, the U-motif, and the

Table 4. Fractional occurrence of branches in the activation network pathway

Main branches connecting the ACT and GATE sites		Fraction of paths (%)								
		RyR1					RyR2			
		C	P	O	O†	I†	C	C†	O†	O
		7k0t	7tzc	7m6l	7tdh	7tdg	7vmm	7ua5	7ua9	7vmp
Name	ATP-site branches									
A1	-CTD – U - ATP - S6-			100		20	100	80		18
A2	-CTD – U - ATP - S6-	60	38						7	21
A3	-CTD – U - ATP - S6-	40								
A4	-CTD – U - ATP - S6-				69					
A5	-CTD - CFF - U - ATP site - S6-									25
A6	-CTD – U - ATP - S45 - S6-					77		20		
	Subtotal	60	38	100	69	97	100	100	7	64
	S45 branches									
A7	-CTD - U - S45 - S6-				14					
A8	-CTD - U - S45 - S6-								93	
	Subtotal	0	0	0	14	0	0	0	93	0
	CFF-site branch									
A9	-CTD - CFF– U - S6-		61		17					36
	Subtotal		61		17					36
	TOTAL	100	99	100	100	97	100	100	100	100

ACT and GATE are defined in Table 8. The abbreviations CTD, U, ATP, CFF, S45, and S6 refer to the Central domain, U-motif, ATP-binding site, CFF-binding site, S45 linker, and S6 helix, respectively, which contribute by one or more residues to the path (see Supplementary Table S3 for the list of critical residues of individual branches).

† marks a pair of RyR1 and RyR2 structures obtained in the same experiment.

537 S6 helix. Six branches involved one or more residues of the ATP-binding site, two branches involved
538 residues of the caffeine/xanthine binding site known to support the calcium-dependent activation (des
539 Georges et al., 2016; Chirasani et al., 2022), and three branches involved residues of the S45 linker
540 known to participate in the regulation of channel gating (Murayama et al., 2011; Gomez et al., 2016).
541 Individual model structures contained 1 – 4 branches in various proportions. One RyR1 and one RyR2
542 structure contained just a single activation branch.

543 Interaction between the calcium activation and calcium inhibition networks.

544 The model RyR structures and their interacting pathways are correlated in Table 5 (the complete list of
545 the critical residues is given in Supplementary Table S4). Each of the six intra-monomeric inhibition
546 branches interacts with at least one activation branch. The largest number of interactions occurs in
547 branch I1, which interacts with 4 activation branches in 2 RyR1-O, 1 RyR1-P, 2 RyR2-C, and 1 RyR2-O
548 structures. The smallest number of interactions occurs in branches I2 and I3, which interact only with A2
549 and only in the RyR2-O structure 7ua9, which does not present other interactions. On the other hand,
550 the activation branch A2 interacts with 3 inhibition branches in 1 RyR1-C, 1 RyR1-P, and 2 RyR2-O

551 structures. Branches I7 – I9 and branch A9 presented no interactions in the allosteric network. A
552 systematic interaction pattern for branches and structures was best revealed when the branches of the
553 networks were connected graphically (Figure 8).

554 **Table 5. Interactions between pathways of the activation and inhibition network.**

	A1	A2	A3	A4	A5	A6	A7	A8	A9
I1	RyR1-O 7m6l$ RyR2-C 7vmm$ RyR2-C 7ua5$ RyR2-O 7vmp$	RyR1-P 7tzc RyR2-O 7vmp		RyR1-O 7tdh	RyR2-O 7vmp				
I2		RyR2-O 7ua9							
I3		RyR2-O 7ua9							
I4	RyR1-I 7tdg	RyR1-P 7tzc				RyR1-I 7tdg$ RyR2-C 7ua5$			
I5				RyR1-O 7tdh					
I6		RyR1-C 7k0t	RyR1-C 7k0t	RyR1-O 7tdh			RyR1-O 7tdh$		
I7									
I8									
I9									
I10						RyR1-I 7tdg#			
I11						RyR1-I 7tdg#			
I12								RyR2-O 7ua9$#	

555 $ marks structures where the same residue of the ATP-binding site or the S45 linker, participates in both the
556 inhibition and activation network.
557 # marks the interaction of the inter-monomeric inhibition pathway with the activation pathway of the
558 anticlockwise-neighboring monomer.
559

560 A search for important residues in the allosteric network revealed several residues shared by both
561 networks. Each analyzed RyR structure involved U-motif residues I4218 and F4219 in either the
562 inhibition allosteric network (7tdh, 7tzc, 7ua9), or the activation allosteric network (7tdg and 7k0t), or
563 both (7m6l, 7vmm, 7ua5, 7vmp). In all RyR structures except RyR1-C 7k0t and RyR2-O 7ua9, at least one
564 branch of the allosteric network contained the U-motif residues K4214 and W4205. In all RyR structures
565 except RyR1-C 7k0t and RyR2-O 7ua9, the activation and inhibition branches converged either before or
566 at these U-motif residues, or in the case of 7tdh at the CTD residue Q4947 that follows the U-motif
567 residue F4219 in the pathway. Thus the U-motif residues I4218, F4219, K4214, and W4205 emerge as
568 essential for the allosteric interaction between the activation and inhibition pathways. The residues
569 I4218 and K4214 also participate in the ATP binding site.

570 In all model structures, the majority of activation and inhibition pathways encompassed at least one
571 ATP-binding residue, therefore these pathways may be speculated to affect the affinity of the ATP
572 binding site and regulation of RyR activity by ATP.

573 It should be underlined that the intra-monomeric pathway of the inhibition network interacts with the
574 activation network in all 9 investigated model structures. The U-motif appears central to mixing signals,
575 incoming from the activation and inhibition sites and passing them through the ATP-binding site, and/or

S45, or directly to the S6 segment. The S6 segment appears central to the signal integration to control the pore open/closed state in all pathways.

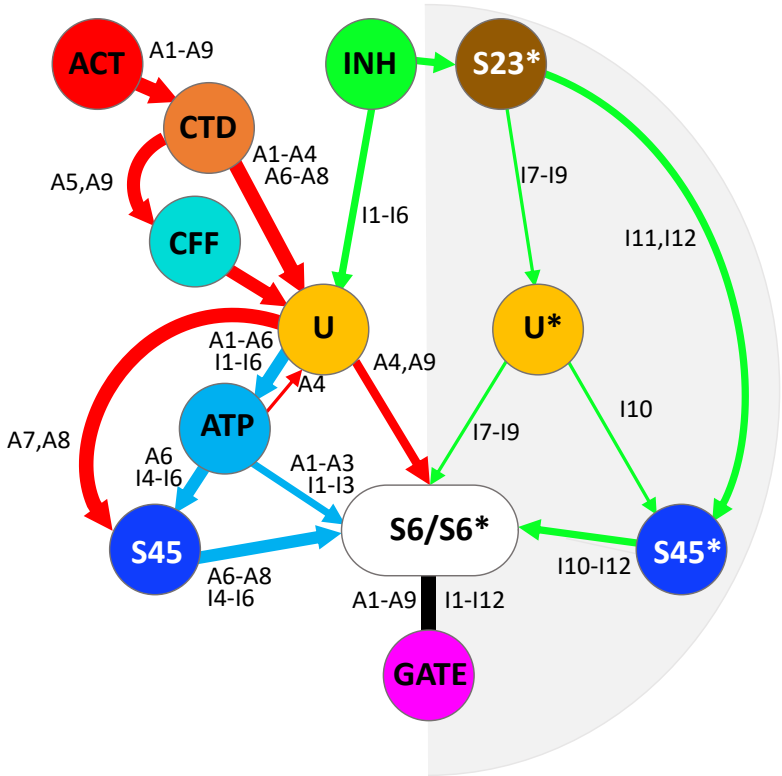

Figure 8. Divalent ion-related allosteric networks of the ryanodine receptor. The scheme integrates the intra-monomeric (white background) and the inter-monomeric pathways (gray background). Note that both pathway types are present in each monomer. Red – the activation network. Green – the inhibition network. Blue – the shared activation and inhibition sub-paths. The branches are labeled in correspondence to Tabs 3 - 5. ACT – the activation site; INH – the inhibition site; CTD – the C-terminal domain; CFF – the caffeine binding site; S23 – the S23 loop; U, U* - the U-motifs; ATP – the ATP binding site; S45, S45* - the S45 linkers; S6/S6* - the S6 helices; GATE - the gating site.

5 Gating model of the RyR1 and RyR2 regulation by divalent ions

The assumed *modus operandi* common to RyR channel isoforms across species should consider the single-channel activity as the result of structural transitions. More specifically, under the given experimental conditions the structural states and their allosteric interactions should have counterparts in the functional states and their allosteric transitions. A theoretical model of the ion-dependent RyR operation based on the results of structural analysis should approximate the single-channel data collected at various concentrations of divalent ions. The experimental structural and functional data indicate that:

(1) The gate structure of the S6 segment is the only structure that controls the permeation state of the channel pore in both RyR1 and RyR2. This means that both the activation and the inactivation processes act on the same gate. Consequently, the activation and the inactivation are inter-dependent processes.

(2) The ion-binding activation site is a self-contained structure composed of equivalent CD and CTD residues in both RyR1 and RyR2. It has a much higher affinity to Ca^{2+} than Mg^{2+} ions, and its allosteric coupling to the channel pore stabilizes the gate in the open state more effectively when occupied by Ca^{2+} than any other ion.

(3) The ion-binding inhibition site is formed by the EF1 and EF2 ion-binding loops in both RyR isoforms. It has a similar low affinity to Ca^{2+} and Mg^{2+} ions, and its allosteric coupling to the channel pore

596 stabilizes the gate in the closed position when occupied by either divalent ion. The binding-to-
597 inactivation allosteric coupling efficiency is higher in RyR1 than in RyR2.
598 (4) RyR isoforms adopt mutually congruent structural and functional macrostates. The bound/unbound
599 state of the ligand binding sites defines the state and the structure of the RyR molecule. The
600 equilibrium between macrostates depends on the concentrations and binding constants of
601 ligands/divalent ions.
602 (5) The closed, primed, and inactivated RyR structures have the gate of all 4 monomers in the closed
603 position. The open RyR structure has the gate of all 4 monomers in the open position.
604 (6) The primed state is defined by activators bound to their respective ATP-binding and/or caffeine-
605 binding sites.
606 (7) The ion-dependent allosteric network of RyR consists of the intra- and inter-monomeric pathways.
607 The intra-monomeric activation and inhibition pathways merge at the U-motif near the ATP and CFF
608 binding pockets. The inter-monomeric pathway is a specialized ion-dependent inhibitory path more
609 prominent in RyR1.
610 (8) The structure of the inactivated RyR2 has not been determined yet; however, it is plausible to
611 suppose that it exists at high concentrations of divalent ions and differs from the inactivated RyR1
612 structure by the extent of EF-hand – S23* coupling.

613 ## Construction of the model of RyR operation

614 The analysis of homotetrameric RyR structures revealed that all four RyR monomers in concord adopt
615 one of four principal structural macrostates – the closed, the primed, the open, and the inactivated. The
616 structure of macrostates depends on the concentrations of divalent ions, ATP, and caffeine. Closed and
617 primed macrostates could be combined into a single closed macrostate of the model since both are
618 closed and cannot be functionally distinguished at a constant ATP concentration. Therefore, we
619 constructed the model of RyR operation, termed the COI model, in which we assigned a functional
620 macrostate corresponding to each of the closed, open, and inactivated structural macrostates (Figure
621 11A). The three macrostates were interconnected so that each could be directly transformed into
622 another since each state was observed at a range of calcium concentrations. As in our previous RyR
623 gating models (Zahradnik et al., 2005; Zahradnikova et al., 2010; Iaparov et al., 2022), transitions
624 between channel states were considered spontaneous, with the unliganded RyR preferring strongly the
625 closed state. A transition between macrostates transpires as a cooperative conformational change of all
626 four monomers that occurs even without ligand binding, albeit with low probability. The binding of
627 ligands changes the relative energies of macrostates, thus also the likelihood of finding the channel in a
628 particular macrostate.

629 In the equilibrium, the probability of occurrence of a macrostate is given by the respective equilibrium
630 constants and allosteric factors. Allosteric factors multiply equilibrium constants to reflect the changes
631 in the energy of a macrostate relative to the closed macrostate, caused by the binding of an ion. If the
632 affinity of an ion to the new macrostate does not change, the allosteric factor is 1, if the affinity
633 increases the factor is <1; and if the affinity decreases the factor is >1. Transitions between states were
634 characterized in the COI model by allosteric factors of two types – allosteric coefficients and interaction
635 factors. The allosteric coefficients define the binding affinity of a single ligand to the O and I macrostates
636 relative to the ligand's affinity in the closed macrostate. The allosteric coefficients of Ca^{2+} and Mg^{2+}

binding at the activation site are defined as f_{Ca} and f_{Mg} in the open macrostate, and h_{Ca} and h_{Mg} in the inactivated macrostate. The inhibition site does not discriminate between Ca^{2+} and Mg^{2+}, therefore the allosteric coefficient is defined as f_M in the open macrostate and h_M in the inhibited macrostate. The interaction factors reflect the changes of ion affinity induced by the simultaneous occupation of both the activation and inhibition sites and are defined as g_{CaM} and g_{MgM} in the closed macrostate, f_{CaM} and f_{MgM} in the open macrostate, and h_{CaM} and h_{MgM} in the inactivated macrostate.

Derivation of the model open probability equation

In the COI model, the equilibrium probability of the open state, P_O, can be described by Eq. 2, using the approach of statistical mechanics (Marzen et al., 2013):

$$P_O = \frac{\frac{1}{K_{O0}} w_O^4}{\frac{1}{K_{O0}} w_O^4 + w_C^4 + \frac{1}{K_{I0}} w_I^4}, \qquad \text{(Eq. 2)}$$

where w_O, w_C, and w_I are the statistical weights of the open, closed, and inactivated macrostates, respectively; the exponent 4 reflects the cooperative action of 4 monomers, and K_{O0} and K_{I0} are the equilibrium constants of the open and the inhibited ligand-free macrostate, respectively.

Changes in RyR states induced by the binding of ions are expressed through the dependences of w_O, w_C, and w_I on the ion-binding equilibria. The weight factors of the resulting COI model, calculated according to Marzen et al. (2013) and Horrigan and Aldrich (Horrigan and Aldrich, 2002), are then given by:

$$w_C = 1 + \frac{[Ca]}{K_{Ca}} + \frac{[Mg]}{K_{Mg}} + \frac{[Ca+Mg]}{K_M} + \frac{[Ca][Ca+Mg]}{g_{CaM}K_{Ca}K_M} + \frac{[Mg][Ca+Mg]}{g_{CaM}K_{Mg}K_M},$$

$$w_O = 1 + \frac{[Ca]}{f_{Ca}K_{Ca}} + \frac{[Mg]}{f_{Mg}K_{Mg}} + \frac{[Ca+Mg]}{f_M K_M} + \frac{[Ca][Ca+Mg]}{f_{CaM}f_{Ca}K_{Ca}K_M} + \frac{[Mg][Ca+Mg]}{f_{MgM}f_{Mg}K_{Mg}K_M},$$

$$w_I = 1 + \frac{[Ca]}{h_{Ca}K_{Ca}} + \frac{[Mg]}{h_{Mg}K_{Mg}} + \frac{[Ca+Mg]}{h_M K_M} + \frac{[Ca][Ca+Mg]}{h_{CaM}h_M K_{Ca}K_M} + \frac{[Mg][Ca+Mg]}{h_{MgM}h_M K_{Mg}K_M}. \qquad \text{(Eqs. 3)}$$

The terms at the right side of the equations characterize individual ion-binding transitions of a monomer. The meaning of individual parameters was defined previously and is specified in Figure 9.

The paucity of single-channel data and the simple shapes of Ca^{2+}- and Mg^{2+}-dependences of open probabilities do not allow determination of all parameters of Eqs. 3. To simplify the solution of Eqs. 3, while still reflecting the observed allosteric pathways, we have used the following assumptions: The allosteric effect of Ca^{2+} and Mg^{2+} bound at the activation site occurs only in the open macrostate, i.e., the h_{Ca} and h_{Mg} values equal 1. The allosteric effect of M^{2+} at the inhibition site occurs only in the inactivated macrostate, i.e., $f_M = 1$. The interaction between the activation and the inhibition site occurs only in the inactivated macrostate, i.e., the interaction factors f_{CaM}, g_{CaM}, f_{MgM}, and g_{MgM} equal 1. Now, Eqs. 3 can be simplified to Eqs. 4:

$$w_C = 1 + \frac{[Ca]}{K_{Ca}} + \frac{[Mg]}{K_{Mg}} + \frac{[Ca+Mg]}{K_M} + \frac{[Ca][Ca+Mg]}{K_{Ca}K_M} + \frac{[Mg][Ca+Mg]}{K_{Mg}K_M},$$

667 $$w_O = 1 + \frac{[Ca]}{f_{Ca}K_{Ca}} + \frac{[Mg]}{f_{Mg}K_{Mg}} + \frac{[Ca+Mg]}{K_M} + \frac{[Ca][Ca+Mg]}{f_{Ca}K_{Ca}K_M} + \frac{[Mg][Ca+Mg]}{f_{Mg}K_{Mg}K_M},$$

668 $$w_I = 1 + \frac{[Ca]}{K_{Ca}} + \frac{[Mg]}{K_{Mg}} + \frac{[Ca+Mg]}{h_M K_M} + \frac{[Ca][Ca+Mg]}{h_{CaM}h_M K_{Ca}K_M} + \frac{[Mg][Ca+Mg]}{h_{MgM}h_M K_{Mg}K_M}. \quad \text{(Eqs. 4)}$$

669 ### Relationship between the COI model and RyR allosteric pathways

670 The operational scheme in Figure 9 describes transitions between (A) and within (B, C, D) individual
671 macrostates respecting the identified allosteric pathways (A1-A9; I1-I12; Figure 10) as described by Eqs.
672 4. The activation allosteric coefficients f_{Ca} and f_{Mg} specify the effect of divalent ion binding to the Ca^{2+}-
673 activation site on the coupling efficiency of the activation pathway (A1-A9). The interaction factor h_{CaM}
674 quantifies the interaction between the activation site and the inhibition site resulting from the existence
675 of common sub-paths in the intra-monomeric network (A1-A6; I1-I6). Since both the activation pathway
676 and the intra-monomeric inhibition pathway lead through the binding site for ATP, the values of f_{Ca}, f_{Mg},
677 h_{CaM}, and h_{MgM} should depend on the binding of ATP; however, since only the absence of ATP or a single
678 concentration of ATP was considered here, its effect was convolved into the respective allosteric factors,
679 which were allowed to depend on the presence of ATP. To reduce the number of parameters (see
680 above), the interaction between the activation and inhibition binding sites in the COI model was
681 constrained only to the inhibited macrostate, as depicted in Figure 9 D.

682 The inactivation allosteric coefficient h_M specifies the impact of divalent ion binding to the RyR inhibition
683 site on the gating site, transmitted through the S23* loop of the neighbor monomer. Since the inter-
684 monomeric inhibition pathway does not involve any ATP-binding residues, the value of h_M is
685 independent of the presence of ATP at either monomer.

686 ## 6 Description of RyR operation by the COI model

687 The experimental data on the dependence of RyR1/ RyR2 open probability on concentrations of $Ca^{2+}$and
688 Mg^{2+} were taken from those published single-channel experiments (Fill et al., 1991; Chu et al., 1993;
689 Zahradnikova et al., 2003; Tencerova et al., 2012; Li et al., 2013) that conformed with conditions used
690 for collecting RyR molecules for cryo-electron microscopy determination of their structure. These
691 include isolated cardiac microsomal vesicles incorporated into lipid bilayers either under near-
692 physiological conditions with a total ATP concentration of 2 - 3 mM, free Mg^{2+} in the range of 0 - 1.3
693 mM, and free Ca^{2+} in the range of 0.1 – 100 µM at the cytosolic side and 0.1 - 1 mM at the luminal side
694 (rat or canine cardiac microsomes (Zahradnikova et al., 2003; Tencerova et al., 2012; Li et al., 2013)) or
695 under simpler conditions in the absence of Mg^{2+} and ATP, at free cytosolic Ca^{2+} in the range of 0.1 –
696 4000 µM and approximately 10 µM luminal Ca^{2+} (canine cardiac microsomes and rabbit or human
697 skeletal muscle microsomes (Fill et al., 1991; Chu et al., 1993)).

698 The published data on Ca^{2+} and Mg^{2+} dependence of the open probability of RyR1 and RyR2 are quite
699 limited by the range, completeness, and compatibility of experimental conditions. To collect enough
700 experimental data on RyR open probability for approximation by the model, we combined published
701 data into three groups (Table 6, and Figure 10 A, B, C). We supposed that the differences in recording
702 conditions surpass possible interspecies differences in the single-channel RyR activity. We combined

data obtained in rat (Tencerova et al., 2012; Li et al., 2013) and canine (Zahradnikova et al., 2003) RyR2 channels in the presence of ATP, luminal Ca^{2+}, and at various cytosolic Ca^{2+} and Mg^{2+} levels, to estimate the parameters of RyR2 transitions at near-physiological conditions (Table 6, "RyR2 + ATP"). The data from canine RyR2 (Chu et al., 1993) in the absence of Mg^{2+} and ATP and at a low level of luminal Ca^{2+} formed the group "RyR2 – ATP" (Table 6). We combined human (Fill et al., 1991) and rabbit (Chu et al., 1993) RyR1 in the absence of Mg^{2+} and ATP and at a low level of luminal Ca^{2+} (Table 6, "RyR1 – ATP"). The groups "RyR1 – ATP" and "RyR2 – ATP" allowed us to characterize the difference between RyR1 and RyR2 channels. The groups "RyR2 + ATP" and "RyR2 – ATP" allowed us to characterize the effect of ATP on RyR2.

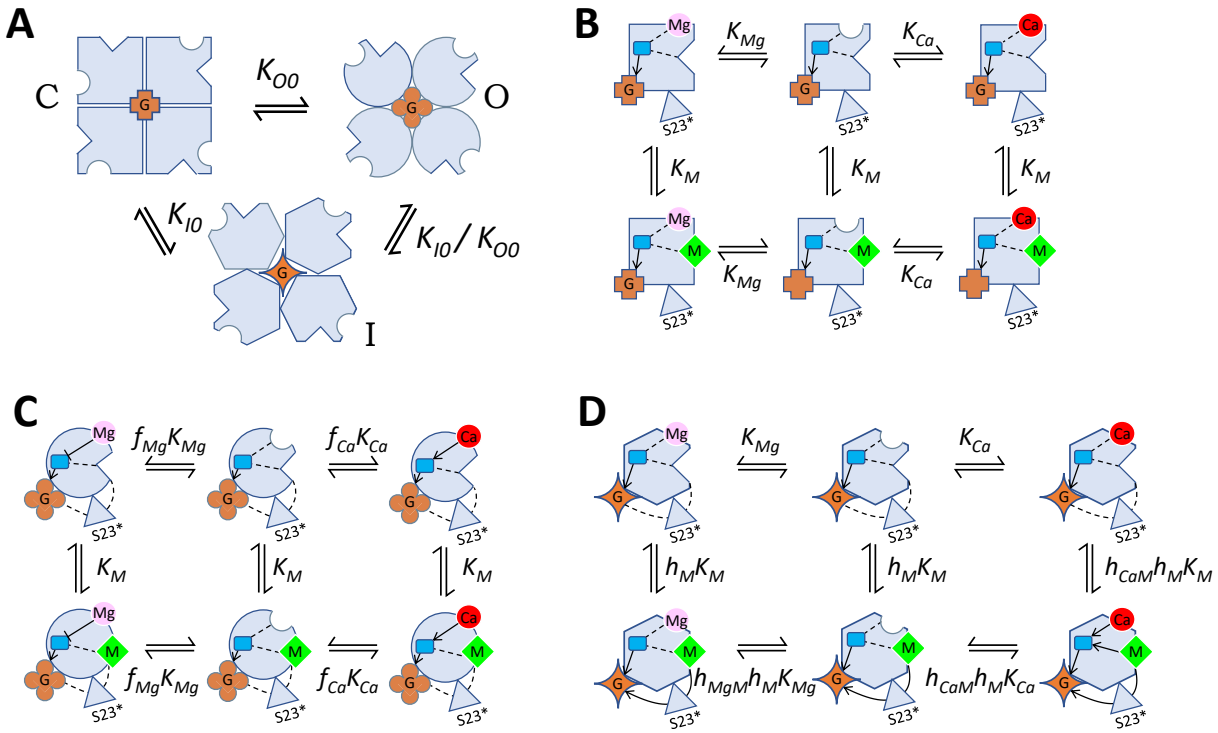

Figure 9. The COI model of RyR channel operation. A: Transitions between the closed, open, and inactivated macrostates of ligand-free RyR with the respective equilibrium constants. Equilibrium constants of transitions between the respective macrostates are indicated. **B:** The ligand-binding transitions of a monomer in the closed macrostate. **C:** The ligand-binding transitions of a monomer in the open macrostate. **D:** The ligand-binding transitions of a monomer in the inactivated macrostate. **B – D:** Gray shapes represent RyR monomers in the respective macrostates as depicted in A. Equilibrium constants of transitions between the respective states are indicated. Lines and arrows represent the allosteric interaction pathways. Dashed lines - no allosteric regulation. Blunt arrow (⊢) - negative allosteric interaction. The pointed arrows (←) - positive allosteric interaction. Round groove – the activation site. Pointed groove – the inhibition site. Blue square – the interaction site of the activation and the intra-monomeric inhibition pathways (ATP-binding site). Red circles – Ca^{2+}; pink circles – Mg^{2+}; green diamonds – M^{2+} (Ca^{2+} or Mg^{2+}). Brown shapes labeled G - the channel pore with the gate in the closed, open, or inactivated state. The grey triangle represents the S23 loop of a neighboring monomer. **D**: The allosteric coefficient h_M is smaller in RyR1 than in RyR2.

The whole combination of datasets, consisting of 54 mean values weighted by their SEMs (Figure 10), was fitted using the same set of equations (Eqs. 4). The values of K_{OO}, f_{Mg}, and K_M, estimated in our previous study based on a principally similar allosteric gating model of RyR2, see (Iaparov et al., 2022), were shared for all three datasets. The stability constant of the unoccupied inactivated state (K_{IO}) was *a*

716 *priori* considered equal to that of the unoccupied open state (K_{O0}). The parameter h_{MgM} could not be
717 optimized for any isoform, due to the interdependence between h_M and h_{MgM} in RyR2 and the absence
718 of data in the presence of Mg^{2+} for RyR1. However, variation of h_{MgM} for RyR2 between 1 and 0.2
719 showed a negligible impact on χ^2 (5%) and coefficient of determination (0.3%), increased the optimal
720 value of K_{Mg} by 9%, of h_{CaM} for RyR2 by 4%, and did not affect the remaining parameters. Therefore h_{MgM}
721 was set to 1 for the final fit. Furthermore, the parameter h_M for RyR2 was set to 1 in correspondence to
722 the small intensity of the inter-monomeric pathway in RyR2 (Table 3). This simplification was tested by
723 varying h_M of RyR2 in the interval $0.25 \leq h_M \leq 1$ that showed negligible impact on χ^2 (4%) and coefficient
724 of determination (0.2%), a proportional change in h_M of RyR1, a reciprocal change in h_{CaM} of both RyR1
725 and RyR2, and undetectable change in the remaining parameters. This interdependence means that the
726 dataset does not allow the determination of the unequivocal values of h_M and h_{CaM} but only of their
727 product $h_M.h_{CaM}$ (Table 6, bottom line). The model parameters h_{CaM} for the datasets "RyR2 – ATP" and
728 "RyR1 – ATP", if optimized as independent parameters, were not significantly different but the
729 parameters h_M and h_{CaM} were highly correlated and their standard errors of the fit were large; therefore,
730 they were shared for the final optimization. In the end, eight parameters of the COI model were set free
731 for fitting the experimental data, as summarized in Table 6. It should be noted that the minimization
732 criterion was the minimal chi-square value for the whole dataset.

733 The solutions of the COI model for the dependences of the RyR1 and RyR2 open probabilities on
734 concentrations of Ca^{2+} and Mg^{2+} ions (Figure 10, lines; Table 6, parameter values) indicate that the
735 model complies satisfactorily with the data obtained at a wide range of conditions. These include four
736 species, two RyR isoforms, and the presence or absence of cytosolic ATP, Mg^{2+}, and luminal Ca^{2+} ions.

737 **Table 6. The best-fit parameters of the COI model.**

Parameter	RyR2 + ATP	RyR2 - ATP	RyR1 - ATP	Reference/justification
K_{O0}	**10 800**			(Iaparov et al., 2022)
K_{Ca} (μM)	0.59 ± 0.15			
K_{Mg} (μM)	36.3 ± 4.3			
f_{Ca}	0.029 ± 0.005	0.10 ± 0.003	0.15 ± 0.01	
f_{Mg}	**3.25**			(Iaparov et al., 2022)
K_{I0}	**10 800**			Equal to K_{O0}
K_M (μM)	**546**			(Iaparov et al., 2022)
h_M	**1**		0.28 ± 0.10	
h_{CaM}	0.016 ± 0.003	0.11 ± 0.04		
COD	0.953			
$h_M.h_{CaM}$	*0.016 ± 0.003*	*0.11 ± 0.04*	*0.031 ± 0.11*	*assuming normal distribution*

738 Values in bold font were taken from (Iaparov et al., 2022) and fixed in all calculations. Values
739 presented as the mean ± error represent the best-fit values and the standard error of the fit. COD
740 – coefficient of determination. Parameters in the column "RyR2 + ATP" correspond to fits to the
741 black and green data points in Figure 10 A and B. Parameters in columns "RyR2 - ATP"
742 correspond to fits to the black data points in Figure 10 C. Parameters in columns and "RyR1 -
743 ATP" correspond to fits to the blue and red data points in Figure 10 C.

744 As mentioned above, the allosteric inhibition factor h_M was fixed to 1 for fitting RyR2 data; this means
745 that the inter-monomeric inhibition pathway was made independent of the occupation of the inhibition
746 site by M^{2+}. Still, however, the intra-monomeric inhibition pathway is operational and RyR2 inactivation

is thus controlled by the interaction factor h_{CaM}, which affects the open probability when the activation site is occupied by Ca^{2+} and the inhibition site is occupied by Ca^{2+} or Mg^{2+} (Figure 9 D). In other words, the simultaneous occupation of both the activation and the inhibition site by divalent ions makes the inhibited macrostate energetically more favorable also in RyR2. Therefore, due to the interaction of the intra-monomeric inhibition pathway with the activation pathway, the reduction of P_O can occur even without the recruitment of the inter-monomeric pathway; the strength of this interaction, h_{CaM}, determines the sensitivity to inhibition by divalent ions in both RyR isomers.

The analysis of inactivation parameters of RyR1 and RyR2 (Table 6) shows that in the absence of ATP, the overall inactivation (proportional to $1/(h_M.h_{CaM})$) is 3.5× more effective in RyR1 than in RyR2 (0.11/0.031 = 3.5). In the presence of ATP and luminal Ca^{2+}, the inactivation of RyR2 is about 7× more effective than in the absence of ATP (0.11/0.016) = 6.9). The relative efficacy of inactivation in RyR1 and RyR2 as well as in the absence and presence of ATP were not affected by the h_M value set for RyR2. However, this value strongly affected the predicted efficacy of the inter-monomeric inhibition pathway relative to the intra-monomeric one. The relative importance of the inter-monomeric pathway increased with inverse proportion to the square of the set value of h_M.

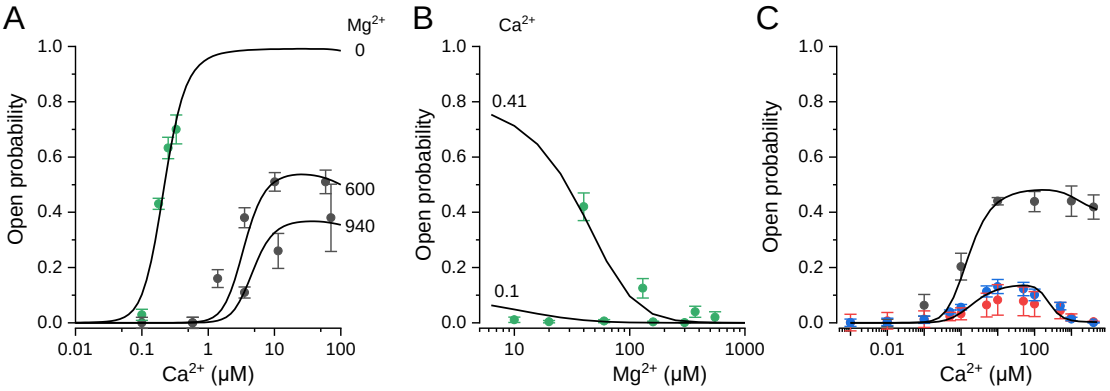

Figure 10. Description of RyR open probability data by the COI model of RyR operation. The data points represent the mean and SEM of the single-channel open probability values read from the referenced publications (see below). The curves represent the theoretical predictions of the COI model (Eqs. 4) with the corresponding parameters for individual data groups in Table 6. **A** – Calcium dependence of the single-channel P_O at cytosolic [Mg^{2+}] of 0, 600, and 940 μM (indicated next to the data) in the presence of 3 mM cytosolic ATP and 1 mM luminal Ca^{2+}. Black points – canine RyR2 channels (Zahradnikova et al., 2003). Green points - rat RyR2 channels (Tencerova et al., 2012). Lines - theoretical predictions of the COI model with parameters for the "RyR2 + ATP" group in Table 6. **B** – Magnesium dependence of the single-channel P_O at cytosolic [Ca^{2+}] of 0.1 and 0.41 μM (indicated next to the data) in the presence of 3 mM cytosolic ATP and 1 mM luminal Ca^{2+}. Green points - rat RyR2 channels (Tencerova et al., 2012; Li et al., 2013). Lines - theoretical predictions of the COI model with parameters for the "RyR2 + ATP" group in Table 6. **C** – Calcium dependence of the single-channel open probability obtained in the absence of cytosolic ATP and Mg^{2+} and with 10 μM luminal Ca^{2+} (Fill et al., 1991; Chu et al., 1993). Black points - canine RyR2 channels (Chu et al., 1993). Blue points - human RyR1 channels (Fill et al., 1991). Red points – rabbit RyR1 channels (Chu et al., 1993). Lines - theoretical predictions of the COI model with parameters for the "RyR1 - ATP" or "RyR2 - ATP" groups in Table 6.
It should be noted that only f_{Ca} and h_M were allowed to vary with the isoform of RyR, while f_{Ca} and h_{CaM} were allowed to vary with the presence of ATP, see their best-fit values in Table 6. All equilibrium constants (K_{O0}, K_{Ca}, K_{Mg}, K_{I0}, K_M) had common values for the whole dataset (Table 6).

In the COI model, the Ca^{2+} and Mg^{2+} dissociation constants of the activation site (K_{Ca}, K_{Mg}, Table 6) as well as the M^{2+} dissociation constant of the inhibition site (K_M, Table 6) are the same for RyR1 and RyR2

764 independent of the species. Independent of the species is also the allosteric factor f_{Ca} controlling the
765 maximum open probability and the apparent sensitivity to activation by Ca^{2+}; however, it is significantly
766 different in RyR1 and RyR2 as well as in the absence and presence of ATP in the case of RyR2 (Table 6).
767 Moreover, the interaction factor h_{CaM} is independent of the species and the RyR isoform in the absence
768 of ATP, and it is the same for RyR2 in both species in the presence of ATP. In this sense, the COI model
769 unifies the published single-channel data on RyR activity, which appeared inconsistent among isoforms,
770 species, and experimental conditions.

Discussion

To elucidate the mechanism of RyR operation, we compared the structures and the activity profiles of RyR1 and RyR2 channels at a range of cytosolic Ca^{2+} and Mg^{2+} concentrations. Examination of the EF-hand region as a candidate divalent ion-binding inhibition site in RyR1 and RyR2 structures indicated that in both isoforms the EF1 and EF2 have a similar predisposition to bind M^{2+}; thus the difference between RyR isoforms in the propensity to inactivation by divalent ions should reside in the transmissibility of the M^{2+} binding signal from the inhibition site to the channel gate. Structural analysis of 26 RyR1 and 17 RyR2 structures revealed a single major difference in the configuration of RyR1 and RyR2 domains that resided in the orientation of the EF-hand relative to the S23 loop of a neighbor monomer (Figures 4 and 5). Other domains in the core RyR structures differed in their positions in the closed state relative to that in the open, primed, or inactivated states; nevertheless, they were similar in RyR1 and RyR2. These facts allow us to conclude that the EF1 and EF2 loops represent the inhibitory M^{2+} binding site in both RyR isoforms since they bind divalent ions well, and the interaction between the EF-hand region and the S23 loop is stronger in RyR1 than in RyR2. Thus, the difference in the inactivation of RyR1 and RyR2 by M^{2+} appears to be explainable simply by the different electrostatic interactions of their EF-hands with the S23* loops specific for RyR isoforms.

The situation turned even more interesting in the analysis of the allosteric network between the divalent ion-binding inhibition site and the gate and between the Ca^{2+}-binding activation site and the gate. This revealed two major pathways in the core structure of both RyR isoforms. The robust intra-monomeric pathway that shares the inhibition and the activation branches and involves residues of the U-motif near and including the ATP- and caffeine-binding sites was present in each of the closed, open, primed, and inactivated structural states. The less robust inter-monomeric pathway, present in all open, primed, and inactivated structural states of RyR1 and one open state of RyR2, uses the connection between the EF-hand region and the S23 loop of neighbor monomers. Both pathways may spread the inhibition signal to the common channel gate at the S6 helix either directly from the U-motif or via the S45 linker (Figure 8).

The question of how this complex structure may fulfill the RyR function was approached by mathematical modeling. We built an operational model based on structural data and applied it to the set of published single-channel data on the RyR channel open probability, measured under similar near-physiological conditions as the analyzed RyR structures. The operation model was built on the premise of the identity of structural and functional macrostates. We postulated the COI model with the closed, open, and inactivated, mutually connected macrostates, and with relative occupancy of the macrostates controlled by ion-binding equilibria among them. The primed state was not resolved from the closed macrostate. Each macrostate has the activation and inhibition divalent ion binding sites and reaction paths obeying the major allosteric pathways. The probability of the COI model reaching the open macrostate depends on the concentration of divalent ions, their respective binding constants, and four allosteric coefficients that regulate the transitions between the channel states. The values of model parameters were found by approximating the experimental dataset of 54 open probabilities from four laboratories, determined at a broad range of Ca^{2+} and Mg^{2+} concentrations, in RyRs isolated from skeletal and cardiac muscles of various mammals. We considered the interspecies differences negligible for simplification. This allowed us to combine the data into three groups with the number of data points

allowing the approximating algorithms to converge to acceptable solutions. After the optimization of the parameter set, the COI model simulation provided reasonable correspondence to experimental data points.

The basic features of the COI model, common to RyR1 and RyR2, are the activation site with a high affinity for Ca^{2+} and a low affinity for Mg^{2+} and the inhibition site with a low affinity for both Ca^{2+} and Mg^{2+}. The difference is in the values of some allosteric parameters that were dependent on either the RyR isoform or the presence/absence of ATP. The allosteric strength of Ca^{2+} binding to the activation site for opening the gate was higher in RyR2 than in RyR1; the allosteric strength for closing the gate by M^{2+} binding to the inhibition site was higher in RyR1 than in RyR2; but the interaction between the inhibition and activation sites was identical in RyR1 and RyR2. The presence of ATP and luminal calcium transpires as the increase in both the activation strength of Ca^{2+} and the interaction strength between the inhibition and the activation site.

Comparison with previous studies

This is the first study that addresses structural relationships related to divalent ion control of RyRs using a large set of structures. Previously, many authors made illuminating discoveries based primarily on a limited set of structures (Bai et al., 2016; Chi et al., 2019; Iyer et al., 2020; Kobayashi et al., 2022) or using one structure for each RyR state (Chirasani et al., 2022; Nayak and Samso, 2022). Our approach based on the analysis of a collection of compatible structures allowed generalization of the partial results on the RyR structure and revealed the interaction of allosteric pathways.

The importance of the U-motif residues I4218 and F4219, which we observed in the allosteric networks of most RyR1 and RyR2 model structures is underlined by the finding that the corresponding RyR2 residues I4172 and F4173 were found important for the interaction of the U-motif with the C-terminal domain and S6 helix, respectively (Kobayashi et al., 2022), and their alanine substitution led to the gain of function for RyR2 (Murayama et al., 2011).

Greene et al. (2022) observed in molecular dynamics simulations that the S45 linker of all monomers has to assume the “open” position for the channel to be open, suggesting their intimate involvement with the transitions between macrostates. The residues T4825, I4826, S4828, and S4829, present in several branches of the activation and inhibition networks, were shown to be involved in RyR1 gating (Murayama et al., 2011), and the mutation T4825I was shown to weaken RyR1 inhibition by Ca^{2+} (Gomez et al., 2016). The existence of the inter-monomeric inhibition pathway in the open RyR2 structure 7ua9 and the presence of the functionally important S45 residues corresponding to rRyR1 T4825, I4826, S4828, and S4829 in its allosteric network suggests that the RyR2 channels might potentially be inactivated also through the inter-monomeric pathway. This is in agreement with the satisfactory fit of RyR2 data with h_M reduced to 0.25. Uehara et al. (2017) found that K4821 of S45 is a critical residue at which cytosolic and luminal inputs converge. We have observed this residue both in the activation and inhibition allosteric pathways of the inhibited RyR1 model structure 7tdg and the closed RyR2 structure 7ua5 and the inhibition pathways of three other RyR1 model structures (Supplementary Tables S2, S3). The determination of the role of luminal Ca^{2+} in RyR gating deserves further study, considering the crucial role of the highly dynamic Ca^{2+} content of SR cisternae (Kubalova et al., 2005; Ziman et al., 2010).

To date, allosteric pathways in ryanodine receptors have been examined only in one study (Chirasani et al., 2022). These authors analyzed activation pathways in the closed 5t15, primed 5tap, and open 5tal RyR1 structures (des Georges et al., 2016) and identified allosteric pathways common for the Ca-, ATP-, and caffeine-binding sites. Our results can be compared to those of Chirasani et al. (2022) only partially since we have not included the structures analyzed by Chirasani et al. (2022) in our analysis due to their lower resolution than the later structures 7m6l and 7tzc (Melville et al., 2022a; Melville et al., 2022b). In the RyR1-C structure 5t15 (des Georges et al., 2016), Chirasani et al. (2022) identified in the Ca-activation network several residues that we identified in the RyR1-C structure 7k0t (Nayak and Samso, 2022): the CTD residue Y4994, the U-motif residue F4217, and the S6 segment residues Q4946 and E4942. The ATP-binding residue I4218 present in the activation pathway of 7k0t occurred only in a less important pathway of 5t15. The incomplete residue conformity in allosteric pathways may be caused by the occupation of the ATP-binding site by ACP in the structure 7k0t, and the empty ATP-binding site in 5t15. In the case of the open RyR1 structures, Chirasani et al. (2022) observed in the Ca activation pathway of 5tal (des Georges et al., 2016) the important ATP-binding residues K4214 and I4218, the CTD residues K4998 and Y4994, and the S6 segment residues Q4946, E4942, and D4938 leading to the gate as we observed in the structure 7m6l (Melville et al., 2022b). The subtle differences between our and the Chirasani's et al. (2022) study might be either due to the differences in the experimental conditions (concentrations of TCEP, ACP vs. ATP, ionic strength) and the limited resolution of the older structures (des Georges et al., 2016).

Chirasani et al. (2023) reported a significant increase of IC50 for inhibition of ^{3}H-ryanodine binding by Ca^{2+} (from ≈0.8 to ≈2.5 mM) and Mg^{2+} (from ≈1.2 to ≈4.5 mM) upon introducing the mutation K4101D into the EF-hand region of RyR1; mutations K4101A and K4101M also had a significant but smaller effect; and mutations of the S23* hydrogen-bonding partner, D4730K or D4730N, did not affect inactivation. In the light of our analysis, these results can be explained by the finding that the allosteric signal can be transmitted from K4101 to both D4730 and I4731 (Supplementary Table S2), and therefore mutation of only one of these residues is not sufficient to block the allosteric transmission through this pathway. Interestingly, the similar K4101E mutation increased the EC50 for Ca^{2+}-dependent activation of ^{3}H-ryanodine binding (Chirasani et al., 2023), difficult to explain for now.

The PDBePISA analysis revealed up to 13 possible different electrostatic interactions (including up to 6 hydrogen bonds) between the EF-hand region and the S23* loop in RyR1 structures. This is in line with the findings of Chirasani et al. (2023) that up to six hydrogen bonds between these domains are formed in molecular dynamics simulations of the open RyR1 structure. The comparison of RyR1 and RyR2 structures in Figure 5 also suggested that the arginine R4736, but not the neutral glycine G4733 and aromatic phenylalanine F4732, is essential for the transmission of the divalent ion binding signal from the EF-hand region to the S23* loop in RyR1. On the other hand, the introduction of the malignant MH mutations G4733E or F4732D decreased RyR1 sensitivity to inactivation to a similar extent as mutations R4736W and R4736Q (Gomez et al., 2016), which was interpreted as a steric effect, not confirmed in our analysis. G4733E and F4732D may have purely electrostatic effects since in both cases an acidic residue was introduced in exchange for a neutral/aromatic residue.

The recent RyR1 structure 7umz, obtained in the presence of 10 mM Mg^{2+}, was defined as the closed state since, since the activation site resembled that in the absence of bound Ca^{2+} despite the presence of

892 a bound Mg^{2+} ion (Nayak et al., 2024). However, the low flexion angle (-2.8°), and the configuration of
893 the EF-hand region relative to the S23 loop reported by (Nayak et al., 2024), as well as in Figure 2 and
894 Figure 3 of this work, resemble the primed and the inactivated state at the same time. The position of
895 the EF-hand region relative to the central domain differs from RyR1 in both the closed and the Ca^{2+}-
896 inactivated states, similar as RyR2 structures (Figure 4). This peculiar conformation can be speculated to
897 result from the independence of the functional macrostate (closed/primed – open – inactivated) from
898 the status of the monomer binding sites, as postulated in the MWC theorem (Monod et al., 1965) and
899 embedded in the COI model. The parameters of the COI model for RyR1 channels in the absence of ATP
900 (Table 6) predict the channel to reside predominantly in the closed state. However, variation of h_{MgM} in
901 the interval between 1 and 0.2, which was shown to be acceptable for RyR2 channels, results in a
902 progressive shift towards the inactivated state (from <1% at h_{MgM} = 1 to ≈80% at h_{MgM} = 0.2). Thus,
903 distinguishing the state of the channel at 10 mm Mg^{2+} would require RyR1 open probability data at a
904 large interval of Ca^{2+}, Mg^{2+}, and ATP concentrations, not presently available.

905 ## Implications

906 The structural analysis presented here explains the paradox of different sensitivity of RyR1 and RyR2 to
907 inactivation by Ca^{2+} (Chu et al., 1993; Laver et al., 1997; Gomez and Yamaguchi, 2014; Gomez et al.,
908 2016) when the Ca^{2+} binding affinity of the EF-hand region of both isoforms is identical (Xiong et al.,
909 1998). Our data showed that the inactivation by divalent ions arises from the same substructures and
910 proceeds by the same mechanism in both RyR isoforms, similar to the activation. In both activation and
911 inactivation, the differences between isoforms emerge from the differences in the strength of the
912 binding signal transmission to the channel gate. According to the COI model, in the case of activation,
913 this influences the allosteric coefficient f_{Ca} that drives RyR opening, which is lower in RyR2 than in RyR1,
914 and thus causes a higher maximum open probability of RyR2. In the case of inactivation, the difference is
915 manifested in the lower allosteric coefficient h_M in RyR1 than in RyR2, which leads to a higher sensitivity
916 to inactivation in RyR1 than in RyR2.

917 The limited data on RyR2 single-channel activity in the presence of ATP suggest that this ligand increases
918 the transmission of the allosteric signal from the activation site, resulting in two effects: An increase of
919 the apparent calcium sensitivity and maximum open probability, evoked by the decrease of the
920 allosteric coefficient f_{Ca}, and an increase of the sensitivity to inactivation (decreased h_{CaM}) caused by the
921 interaction between the Ca^{2+}-bound activation site and the M^{2+}-bound inhibition site. The increased
922 sensitivity of RyR2 to Ca^{2+}-dependent inactivation in the presence of ATP is also supported by single-
923 channel experiments (Gyorke and Gyorke, 1998)(Chu et al., 1993). It can be speculated that the lower f_{Ca}
924 in the presence of ATP is due to the prevalence of the RyR in the primed state since the binding of ATP
925 analogs induces the primed structural macrostate in RyRs (Cholak et al., 2023). The primed state is
926 structurally very close to the open state, and therefore the transitions between them should be
927 energetically less demanding than the transitions between the structurally more different closed and
928 open states. Precise determination of these effects would require expanding the COI model to explicitly
929 include the ATP binding site and the primed state; construction of such a model is at present hampered
930 by the lack of open probability data at a sufficiently wide range of experimental conditions. Since the
931 COI model does not contain explicit ATP-binding transitions, the effect of ATP transpired only through
932 the allosteric parameters f_{Ca} for Ca^{2+}-dependent activation and h_{CaM} for M^{2+}-dependent inactivation.

933 The ATP site-containing branches of the activation pathway (A1 – A6, Table 4) appear responsible for the
934 synergy between the Ca^{2+} and ATP activating mechanisms in all RyR channels, as previously recognized
935 for the primed and open RyR1 structures (Chirasani et al., 2022). Our analysis reveals that this
936 interaction path also exists in the closed RyR structures 7k0t, 7vmm, and 7ua5 with unoccupied Ca^{2+}-
937 binding site, in which the relative position of the C-terminal and Central domains differs from the primed
938 and open channels. This indicates that the molecular backbone for the transmission of the activation
939 allosteric signal is preexistent in all RyR gating states and that the Ca^{2+} binding itself may constitute the
940 signal that promotes the channel activation.

941 ## Limitations

942 The single-channel experiments, used here for deriving the model of RyR operation, were performed
943 under a limited number of experimental conditions that also slightly differed among laboratories. Only
944 experiments under two sets of conditions close to the physiological ones were included in the analysis
945 since RyR activity is sensitive to the ion composition and ionic strength of its environment (Ma et al.,
946 1993; Meissner et al., 1997; Liu et al., 1998). Experiments with purified RyR channels were neither
947 included for their different sensitivity to activation and inactivation by Ca^{2+} (Imagawa et al., 1987).

948 Due to the stochastic nature of the single-channel activity and the limited amount of available data, the
949 precision of some data used in this study might be influenced by natural variance, especially at low open
950 probability conditions. However, sufficiently exact measurements under conditions of low channel
951 activity would require the collection of a large amount of data (Zahradnikova et al., 2020) that might not
952 be experimentally feasible. Therefore, several parameters of the model of RyR operation had to be fixed
953 in this study at previously estimated values (Zahradnik et al., 2005; Iaparov et al., 2022). To determine
954 the relative importance of the intra- and inter-monomeric inhibition pathways would require
955 quantitative data on the effect of Mg^{2+} on RyR1 and RyR2 channels in the absence of ATP.

956 Unfortunately, it was not possible to use experimental data on ^{3}H-ryanodine binding for tuning the COI
957 model of RyR operation. First, the data from many laboratories do not present RyR inactivation, which
958 might be caused by the lengthy experimental procedure or by the presence of higher salt concentrations
959 (Murayama et al., 2018). Second, at least in some laboratories, activation of ^{3}H-ryanodine binding by
960 Mg^{2+} ions was observed (Chugun et al., 2007), an effect that has not been observed in the single-channel
961 measurements. Third, ^{3}H-ryanodine binding data are mostly presented relative to the maximum
962 observed binding, without providing the ^{3}H-ryanodine binding capacity B_{max} that would correspond to
963 the maximum of the channel open probability (P_o = 1).

964 At present, two problems of RyR inactivation have not been solved yet: Regarding the cardiac isoform,
965 no structure of the inhibited RyR2 was published till the present time. Despite observations of over 50%
966 inhibition by Ca^{2+} in the purified RyR2 channel at 10 mM Ca^{2+} in the absence of ATP (Xu et al., 1996), or
967 even at 1 mM Ca^{2+} in the native RyR2 channel in the presence of ATP (Gyorke and Gyorke, 1998), the
968 only RyR2 structure published at 5 mM Ca^{2+} in the presence of ATP and caffeine represented the open
969 and not the inactivated state (Gong et al., 2019). Regarding the skeletal muscle isoform, no electron
970 densities attributable to ions bound at the EF-hand loops were observed either in the Ca^{2+}-inactivated
971 RyR1 (Nayak and Samso, 2022) or the Mg^{2+}-inactivated RyR1 (Nayak et al., 2024). However, the local

resolution of the electron density map is insufficient to decide unequivocally whether Ca^{2+} ions are present or not in the structure of the apparent ion binding inhibition site.

Concluding remarks

The existence of the comprehensive model of mammalian RyR operation puts together the partial observations on RyR structures, equilibrium binding studies, and single-channel gating activity, collected across species and over the years by many independent laboratories.

The methods of bioinformatic analysis applied to numerous RyR structures have shown that in both RyR isoforms, the inhibitory binding site for divalent ions is very likely formed by the EF1 and EF2 loops. The transmission of the inhibition signal to the channel gate proceeds through two pathways: the inter-monomeric pathway that leads through the interface between the EF-hand region and the S23* loop, and the intra-monomeric pathway that converges with the Ca^{2+}-activation pathway. The difference between RyR1 and RyR2 inhibition by divalent ions is caused by the different coupling efficiency of the inhibition pathways in RyR1 and RyR2.

RyR1 and RyR2 structures present a peculiar construction of their core that controls the RyR channel activity in dependence on the cytosolic concentration of Ca^{2+} and Mg^{2+} ions and endogenous modulators like ATP and xanthines. Each RyR monomer has specific binding sites for these ligands connected to the channel gate by a common allosteric network. Changes in the ligand occupation of binding sites drive stochastic transitions of RyR monomers among the closed – primed – open – inactivated macrostates to the energetically preferable state. The macrostate of monomers in the RyR homo-tetramer does change in synchrony, by a structural process supported by the inter-monomeric coupling of allosteric networks. Recent data point to the central role of the U-motif at which the intra-monomeric and inter-monomeric allosteric networks merge and allow for the exchange of energy.

994 # Materials and Methods

995 ## Bioinformatics analyses

996 Ryanodine receptor sequences were taken from the UniProt database (https://www.uniprot.org/) and
997 aligned using CLUSTAL Omega at EMBL-EBI (https://www.ebi.ac.uk/jdispatcher/msa/clustalo; (Sievers et
998 al., 2011)) relative to rabbit RyR1. The residue numbers of the examined domains are given in Table 7 for
999 the studied species/isoforms.

1000 Table 7. Sequence numbers of the ryanodine receptor core domains.

Domain	rRyR1	mRyR2	hRyR2	pRyR2, rRyR2
Central domain (CD)	3668-4070	3634-4024	3635-4025	3636-4026
EF-hand region (EF)	4071-4131	4025-4085	4026-4086	4027-4087
U-motif (U)	4132-4251	4086-4205	4087-4206	4088-4207
S23 loop (S23)	4663-4786	4591-4715	4592-4716	4593-4717
S45 linker (S45)	4821-4834	4750-4763	4751-4764	4752-4765
S6 segment (S6)	4910-4956	4839-4885	4840-4886	4841-4887
C-terminal domain (CTD)	4957-5033	4886-4962	4887-4963	4888-4964

1001 Prefixes r, m, h, and p refer to rabbit, mouse, human, and pig.

1002 Sequence identities of RyR isoforms were calculated using the SIAS server
1003 (http://imed.med.ucm.es/Tools/sias.html). In the text, sequence numbers are given for the rabbit RyR1
1004 (rRyR1) and human RyR2 (hRyR2), if not indicated otherwise.

1005 Structures of ryanodine receptors were obtained from the protein data bank (https://www.rcsb.org/).
1006 To ensure compatibility of structural and functional data, we have considered and used those RyR
1007 structures that were either ligand-free or contained Ca^{2+}-, Mg^{2+}, caffeine (xanthine), ATP (ACP) visible in
1008 their structure or were obtained in the presence of these ligands or their combination (Supplementary
1009 Table S1). These included 26 structures of rabbit RyR1 (des Georges et al., 2016; Melville et al., 2022a;
1010 Melville et al., 2022b; Nayak and Samso, 2022), 7 structures of pig RyR2 (Peng et al., 2016; Gong et al.,
1011 2019), 5 structures of human RyR2 (Miotto et al., 2022) and 5 structures of mouse RyR2 (Kobayashi et
1012 al., 2022). The resolution of these structures was reported in the range of 2.45 - 6.2 Å. Structures of
1013 mutant RyRs, or structures obtained in the presence of ryanodine, ruthenium red, or the activator
1014 pentachlorobiphenyl, and structures with unresolved critical amino acid side chains were not included.

1015 The flexion angle between the horizontal plane and the line formed by Cα atoms of residues
1016 corresponding to rRyR1 residues 348 and 1052 (Steele and Samso, 2019) was measured manually in
1017 Chimera Ver. 1.17 (Pettersen et al., 2004) (https://www.rbvi.ucsf.edu/chimera) and is shown in
1018 Supplementary Table S1.

1019 Editing and optimization of structures were performed in Chimera as follows: The monomer core (the C-
1020 terminal quarter residues 3639 – 5037; (Du and Maclennan, 1999)) or its selected part was cut out from
1021 the whole RyR structure. In model structures used for the determination of allosteric pathways, the
1022 short unresolved loops were reconstructed to correspond to the known sequence, and the missing long
1023 part of the unresolved DR1 region was replaced by a polyglycine loop. The reconstructed loops were

1024 optimized using the program MODELLER (Sali and Blundell, 1993) or the server MODLOOP
1025 (https://modbase.compbio.ucsf.edu/modloop/ (Fiser et al., 2000; Fiser and Sali, 2003)). The edited
1026 structures were repaired by adding missing atoms to incomplete residues. Finally, hydrogens and
1027 appropriate charges were added. Selective residue mutations were introduced to the studied segments
1028 of interest in Chimera.

1029 The repaired model structures were energy-minimized using at least 1000 iterations of steepest descent
1030 and 100 iterations of maximum gradient minimization with fixed positions of the first five and last five
1031 Cα atoms. The resulting model structures were used for different types of analysis as indicated in
1032 Supplementary Table S1.

1033 The maximum distance between Cα atoms of H-bond-forming electron donor residues glutamate or
1034 aspartate and the electron acceptor residues lysine or arginine was calculated as follows: The distance
1035 from the Cα atom to the farthest oxygen atom of the electron donor residue (d_D), and the distance from
1036 the Cα atom to the farthest nitrogen atom of the electron acceptor residue (d_A) in their extended
1037 configurations were measured. The maximum distance was calculated as the sum ($d_D + d_A + 2.7$) Å,
1038 where 2.7 Å is the standard length of a hydrogen bond.

1039 The EF-hand identity score (IS) was calculated according to the scoring system of Zhou et al. (2006),
1040 which compares the identity of amino acids in the ion-binding loop of the examined EF-hand sequence
1041 with the 12 amino acids of the canonical EF-hand loop (EF-hand PROSITE pattern PS00018) or their
1042 allowed equivalents (D, N, S at position 1, and any residue at position 2). The resulting identity score
1043 consists of three numbers x/y/z. The value of x (0 - 12) reports the number of amino acids concurring at
1044 their given positions with amino acids of the allowed EF-hand loop residues. The value of y (0 - 6)
1045 reports the number of amino acids concurring with the 6 amino acids of the loop in positions 1, 3, 5, 7,
1046 9, and 12, involved in divalent ion binding. The value of z (0 - 3) compares the amino acid concurrence at
1047 positions 1, 3, and 12, considered critical for ion binding. Thus, a canonical EF-hand, such as that of
1048 calmodulin, provides the highest EF-hand identity score of 12/6/3. We report the IS together with the
1049 sum of the partial scores in the form of x/y/z (x+y+z).

1050 The ion binding score (IBS) and the number of ion binding poses (NIBP) of EF-hand loops were estimated
1051 on edited and energy-optimized model structures using the MIB2 server
1052 http://combio.life.nctu.edu.tw/MIB2/ (Lu et al., 2022) as follows: first, the EF-hand region and 31
1053 subsequent residues ending with a β-hairpin, corresponding to rabbit RyR1 residues 4032-4182, were
1054 isolated from the selected RyR structures (Supplementary Table S1). This segment was chosen for its
1055 expected structural stability. The optimized EF-hand structure was uploaded to the MIB2 server, which
1056 returned the ion-binding scores for all individual residues and the number of acceptable ion-binding
1057 poses.

1058 Electrostatic interactions as well as the interface area between the interacting EF-hand region and S23
1059 loop were quantified on edited and optimized structures using the server PDBePISA
1060 (https://www.ebi.ac.uk/msd-srv/prot_int/cgi-bin/piserver). The examined structures contained residues
1061 4032-4182 of the extended EF-hand region and residues 4695-4745 of the S23* loop.

1062 Root-mean-square deviations (RMSD) were estimated on unedited original structures in Chimera (Ver. 1.
1063 17). The examined structures were aligned through the Cα atoms of their Central domain residues
1064 (corresponding to rRyR1 residues 3668-3679, 3694-3733, 3753-3855, and 3873-4070, which were
1065 resolved in all RyR structures) with the corresponding Cα atoms of the reference RyR structures 7k0t
1066 (closed RyR1) and 7tdg (inactivated RyR1). The RMSD between Cα atoms of the examined RyR domains
1067 in different structural states and the corresponding Cα atoms of the reference RyR structures were
1068 calculated. RMSD calculation of the S23 loop was performed only on residues 4716-4754, positioned in
1069 the vicinity of the neighbor monomer, since the rest of the S23 loop was not well-resolved in all
1070 structures. Otherwise, the domain residues were specified according to Table 7. The RMSD values were
1071 normalized for 100 amino acid residues (Carugo and Pongor, 2001) to account for differences in the
1072 length of individual domains, and denoted as 7k0t-$RMSD_{100}$ or 7tdg-$RMSD_{100}$ for alignment with 7k0t or
1073 7tdg, respectively. Only $RMSD_{100}$ values larger than 2 Å were considered to indicate a significant
1074 structural change (Carugo, 2007).

1075 Allosteric pathways were traced using the server OHM (https://dokhlab.med.psu.edu/ohm/#/home,
1076 (Wang et al., 2020)). Five RyR1 and four RyR2 structures with the best resolution and the lowest number
1077 of unresolved residues were selected from the studied set (Supplementary Table S1) and processed for
1078 analysis. Two copies of the monomer core were aligned to two adjacent monomers of the original RyR
1079 tetrameric structure. The resulting dimers were subjected to energy minimization in Chimera Ver. 1.17
1080 until all clashes were removed. Finally, the optimized model structures were uploaded to the OHM
1081 server to trace the sequences of residues connecting the allosteric site of interest with the active site. As
1082 the allosteric site, either the residues of the EF1 and EF2 loops (INH) as the putative divalent ion binding
1083 inhibition site or the CD and CTD residues of the Ca^{2+}-binding activation site (ACT) (Wang et al., 2020;
1084 Chirasani et al., 2022) were selected. As the active site, the gate and hinge residues of the S6 segment
1085 (Table 8) were selected.

1086 The output of the OHM server consisted of two items for each RyR structure: 1. The list of the first 100
1087 most important allosteric pathways (“paths.txt”), in which a chain of interacting residues represented
1088 the individual pathway. This list was used for sorting paths by important residues and estimating the
1089 fraction of major pathways and branches. 2. The description of the complete allosteric network
1090 ("net.txt”), consisting of the list of critical residues of the allosteric network with their respective
1091 allosteric coupling intensities (ACI), and the list of network edges, showing connections between the
1092 residues in the pathway. The network list was used to select the residues with the highest ACI and
1093 examine their connections within the pathways. In addition to these outputs, the graph of the allosteric
1094 network for a selected set of pathways (3, 5, 7, 10, 20, 30, 40, 50, 60, 70, 80, 90, or all of the 100 listed
1095 pathways) was visually examined to understand the meaning of different pathways in the context of all
1096 possible pathways. The fractional contribution of critical residues (output list “_net.txt”) functionally and
1097 structurally important to the allosteric network was calculated as the frequency of their occurrence in
1098 the first 100 most frequently occurring pathways (output list “_paths.txt”). The output files “_net.txt”
1099 and “_paths.txt” are located in the file Supplementary_Data.zip.

1100 Table 8. The residues of the allosteric and active sites (rRyR1 numbering)

Allosteric sites	**Residues**
INH: EF-hand loops	4081-4092, 4116-4127
ACT: Ca^{2+} activation site	**3893, 3967**, 3970, **5001**, 5002
Active site	
GATE: S6 Hinge and Gate	G4934, G4934*, I4937, I4937*

1101 Residues with * belong to the monomer neighboring the
1102 monomer bearing the analyzed allosteric site.
1103 Residue numbers in bold were originally defined as the Ca^{2+}
1104 binding site-forming residues by (des Georges et al., 2016).

1105 Modeling the RyR operation

1106 The model of RyR operation was constructed on the Monod-Wyman-Changeaux (MWC) theorem
1107 (Monod et al., 1965) and homo-tetrameric Markovian memory-free mechanism (Zahradnik et al., 2005;
1108 Zahradnikova et al., 2010) using a statistical mechanics approach (Marzen et al., 2013; Iaparov et al.,
1109 2022). The model presumes an allosteric mechanism where ions activating and/or inhibiting RyR
1110 opening bind to the specific regulatory sites present on each monomer and exert their effect by
1111 allosteric coupling to the remote gating site. The gating site of the RyR pore should be in the open
1112 position in all four monomers to make the ion permeation possible. The free energy of ion binding to
1113 the specific binding site is supposed to be independent of the identity of the monomer and the
1114 presence/absence of ligands at the binding sites of other monomers but is supposed to depend on the
1115 macrostate of the whole RyR. Mathematically, all possible macrostates pre-exist in the absence of
1116 ligands and the binding of a ligand affects the relative occurrence of a given macrostate by altering its
1117 free energy. A transition between macrostates occurs in a concerted manner at all monomers (Hilser et
1118 al., 2012). This supposition greatly reduces the number of considered macrostates and reduces demands
1119 on computational power.

1120 The dependence of the RyR open probability on the concentration of regulatory ions was described
1121 using the framework of statistical mechanics (Marzen et al., 2013; Iaparov et al., 2022). The parameters
1122 of the model equations (see Results) were optimized using the Levenberg-Marquardt method for the
1123 best fit of the RyR single-channel open probability data in OriginPro (ver. 2022b). The simple shape of
1124 the calcium dependence of open probability and the limited size of available experimental data led to
1125 the mutual dependence of some fitted parameters and non-convergence of the fit. To solve this
1126 problem, the number of free parameters was reduced as described in the Results. A global fit of the
1127 whole dataset was then performed with the minimal chi-square value as the minimization criterion for
1128 the whole dataset.

1129 Statistical analysis

1130 One-way ANOVA was performed in Origin (OriginLab, V. 2024) to test the significance of the differences
1131 between groups. The test was performed only if the distribution of data did not significantly deviate
1132 from normality (Shapiro-Wilk test), and if the population variances were not significantly different
1133 (Levene's test). Comparison of means was performed with Scheffe's test. Values with $p < 0.05$ were
1134 considered significant. The power of the test was calculated at $\alpha = 0.05$ and had to be > 0.95 to accept

1135 the ANOVA results. If the distribution of data deviated from normality, the Kruskal-Wallis ANOVA
1136 followed by Dunn's test were used instead.

Acknowledgments

The authors would like to thank Dr. N. V. Dokholyan and Dr. V.R. Chirasani for their help with using the OHM server, and to Dr. B. Iaparov for the help with using statistical mechanics.

This work was supported by the Turkish-Slovak Joint Partnership of The Scientific and Technological Research Council of Turkey (TÜBİTAK) and Slovak Academy of Sciences grant JRP/2019/836/RyRinHeart and TÜBİTAK grant number 119Z578, and by the projects APVV-21-0443 from the Slovak Research and Development Agency, and VEGA 2/20182/21 from the Ministry of Education, Research, Development and Youth of the Slovak Republic and Slovak Academy of Sciences.

Author contributions

A.Z. and I.Z. conceived and designed the study; A.Z. supervised the study, created the structural models, performed structural analysis and visualization, and designed, derived, and validated the statistical mechanics model; A.Z. and J.P. performed server-based bioinformatics analysis; A.Z., J.P. and M.S. validated the bioinformatics analysis; S.B. performed molecular simulations and provided valuable intellectual input; A.Z. and I.Z. interpreted the data and wrote the manuscript; S.B. reviewed and edited the manuscript.

Competing interests

The authors declare no competing interests.

Author ORCIDs

Alexandra Zahradníková: https://orcid.org/0000-0002-7296-9617
Jana Pavelková: https://orcid.org/0000-0002-9539-2312
Miroslav Sabo: https://orcid.org/0009-0009-2112-2502
Sefer Baday: https://orcid.org/0000-0002-2913-6687
Ivan Zahradník: https://orcid.org/0000-0001-5125-9467

Supplementary Information

Supplementary Information contains a link to the Supplemental Data, a link to Supplementary Table S1 that lists the structures used in this study and their characteristics as well as the evaluated RyR1/RyR2 open probabilities, Supplementary Tables S2 and S3 listing the important residues of individual branches of the inhibition and activation networks, respectively, and Supplementary Table S4 listing the interactions between the activation and inhibition branches.

Data availability

The data that support this study are available from the corresponding authors upon request. Previously published protein structure data used for analysis in this study are available in the Protein Data Bank under accession codes listed in Supplementary Table S1.

1170 The data output of the OHM server used in the analysis of allosteric pathways is supplied as
1171 Supplemental_Data.zip.

1172 References

1173 Bai, X.C., Z. Yan, J. Wu, Z. Li, and N. Yan. 2016. The Central domain of RyR1 is the transducer for long-
1174 range allosteric gating of channel opening. *Cell Res*. 26:995-1006. doi: 10.1038/cr.2016.89.

1175 Bers, D.M., C.W. Patton, and R. Nuccitelli. 1994. A practical guide to the preparation of Ca2+ buffers.
1176 *Methods Cell Biol*. 40:3-29. doi: 10.1016/s0091-679x(08)61108-5.

1177 Carugo, O. 2007. Statistical validation of the root-mean-square-distance, a measure of protein structural
1178 proximity. *Protein Eng Des Sel*. 20:33-37. doi: 10.1093/protein/gzl051.

1179 Carugo, O., and S. Pongor. 2001. A normalized root-mean-square distance for comparing protein three-
1180 dimensional structures. *Protein Sci*. 10:1470-1473. doi: 10.1110/ps.690101.

1181 Chi, X., D. Gong, K. Ren, G. Zhou, G. Huang, J. Lei, Q. Zhou, and N. Yan. 2019. Molecular basis for
1182 allosteric regulation of the type 2 ryanodine receptor channel gating by key modulators. *Proc*
1183 *Natl Acad Sci U S A*. 116:25575-25582. doi: 10.1073/pnas.1914451116.

1184 Chirasani, V.R., M. Elferdink, M. Kral, J.S. Carter, S. Heitmann, G. Meissner, and N. Yamaguchi. 2023.
1185 Structural and functional interactions between the EF hand domain and S2-S3 loop in the type-1
1186 ryanodine receptor ion channel. *J Biol Chem*.105606. doi: 10.1016/j.jbc.2023.105606.

1187 Chirasani, V.R., K.I. Popov, G. Meissner, and N.V. Dokholyan. 2022. Mapping co-regulatory interactions
1188 among ligand-binding sites in ryanodine receptor 1. *Proteins*. 90:385-394. doi:
1189 10.1002/prot.26228.

1190 Cholak, S., J.W. Saville, X. Zhu, A.M. Berezuk, K.S. Tuttle, O. Haji-Ghassemi, F.J. Alvarado, F. Van Petegem,
1191 and S. Subramaniam. 2023. Allosteric modulation of ryanodine receptor RyR1 by nucleotide
1192 derivatives. *Structure*. 31:790-800 e794. doi: 10.1016/j.str.2023.04.009.

1193 Chu, A., M. Fill, E. Stefani, and M.L. Entman. 1993. Cytoplasmic Ca2+ does not inhibit the cardiac muscle
1194 sarcoplasmic reticulum ryanodine receptor Ca2+ channel, although Ca2+-induced Ca2+
1195 inactivation of Ca2+ release is observed in native vesicles. *Journal of Membrane Biology*. 135:49-
1196 59. doi:

1197 Chugun, A., O. Sato, H. Takeshima, and Y. Ogawa. 2007. Mg2+ activates the ryanodine receptor type 2
1198 (RyR2) at intermediate Ca2+ concentrations. *Am J Physiol Cell Physiol*. 292:C535-544. doi:

1199 Dashti, A., G. Mashayekhi, M. Shekhar, D. Ben Hail, S. Salah, P. Schwander, A. des Georges, A. Singharoy,
1200 J. Frank, and A. Ourmazd. 2020. Retrieving functional pathways of biomolecules from single-
1201 particle snapshots. *Nat Commun*. 11:4734. doi: 10.1038/s41467-020-18403-x.

1202 des Georges, A., O.B. Clarke, R. Zalk, Q. Yuan, K.J. Condon, R.A. Grassucci, W.A. Hendrickson, A.R. Marks,
1203 and J. Frank. 2016. Structural Basis for Gating and Activation of RyR1. *Cell*. 167:145-157 e117.
1204 doi: 10.1016/j.cell.2016.08.075.

1205 Du, G.G., and D.H. Maclennan. 1999. Ca(2+) inactivation sites are located in the COOH-terminal quarter
1206 of recombinant rabbit skeletal muscle Ca(2+) release channels (ryanodine receptors). *Journal of*
1207 *Biological Chemistry*. 274:26120-26126. doi:

1208 Efremov, R.G., A. Leitner, R. Aebersold, and S. Raunser. 2015. Architecture and conformational switch
1209 mechanism of the ryanodine receptor. *Nature*. 517:39-43. doi: 10.1038/nature13916.

1210 Fessenden, J.D., W. Feng, I.N. Pessah, and P.D. Allen. 2004. Mutational analysis of putative calcium
1211 binding motifs within the skeletal ryanodine receptor isoform, RyR1. *J Biol Chem*. 279:53028-
1212 53035. doi: 10.1074/jbc.M411136200.

1213 Fill, M., E. Stefani, and T.E. Nelson. 1991. Abnormal human sarcoplasmic reticulum Ca2+ release
1214 channels in malignant hyperthermic skeletal muscle. *Biophysical Journal*. 59:1085-1090. doi:

1215 Fiser, A., R.K. Do, and A. Sali. 2000. Modeling of loops in protein structures. *Protein Sci*. 9:1753-1773.
1216 doi: 10.1110/ps.9.9.1753.

1217 Fiser, A., and A. Sali. 2003. ModLoop: automated modeling of loops in protein structures. *Bioinformatics*.
1218 19:2500-2501. doi: 10.1093/bioinformatics/btg362.

1219 George, C.H., H. Jundi, N.L. Thomas, D.L. Fry, and F.A. Lai. 2007. Ryanodine receptors and ventricular
1220 arrhythmias: Emerging trends in mutations, mechanisms and therapies. *Journal of Molecular*
1221 *and Cellular Cardiology*. .42:34-50. doi:

1222 Gillespie, D. 2020. Recruiting RyRs to Open in a Ca(2+) Release Unit: Single-RyR Gating Properties Make
1223 RyR Group Dynamics. *Biophys J*. 118:232-242. doi: 10.1016/j.bpj.2019.11.021.

1224 Gillespie, D., and M. Fill. 2013. Pernicious attrition and inter-RyR2 CICR current control in cardiac muscle.
1225 *J Mol Cell Cardiol*. 58:53-58. doi: 10.1016/j.yjmcc.2013.01.011.

1226 Gomez, A.C., T.W. Holford, and N. Yamaguchi. 2016. Malignant hyperthermia-associated mutations in
1227 the S2-S3 cytoplasmic loop of type 1 ryanodine receptor calcium channel impair calcium-
1228 dependent inactivation. *Am J Physiol Cell Physiol*. 311:C749-C757. doi:
1229 10.1152/ajpcell.00134.2016.

1230 Gomez, A.C., and N. Yamaguchi. 2014. Two regions of the ryanodine receptor calcium channel are
1231 involved in Ca(2+)-dependent inactivation. *Biochemistry*. 53:1373-1379. doi:
1232 10.1021/bi401586h.

1233 Gong, D., X. Chi, J. Wei, G. Zhou, G. Huang, L. Zhang, R. Wang, J. Lei, S.R.W. Chen, and N. Yan. 2019.
1234 Modulation of cardiac ryanodine receptor 2 by calmodulin. *Nature*. 572:347-351. doi:
1235 10.1038/s41586-019-1377-y.

1236 Greene, D., M. Barton, T. Luchko, and Y. Shiferaw. 2022. Molecular Dynamics Simulations of the Cardiac
1237 Ryanodine Receptor Type 2 (RyR2) Gating Mechanism. *J Phys Chem B*. 126:9790-9809. doi:
1238 10.1021/acs.jpcb.2c03031.

1239 Guo, W., B. Sun, J.P. Estillore, R. Wang, and S.R.W. Chen. 2020. The central domain of cardiac ryanodine
1240 receptor governs channel activation, regulation, and stability. *J Biol Chem*. 295:15622-15635.
1241 doi: 10.1074/jbc.RA120.013512.

1242 Gyorke, I., and S. Gyorke. 1998. Regulation of the cardiac ryanodine receptor channel by luminal Ca2+
1243 involves luminal Ca2+ sensing sites. *Biophysical Journal*. 75:2801-2810. doi:

1244 Hadiatullah, H., Z. He, and Z. Yuchi. 2022. Structural Insight Into Ryanodine Receptor Channelopathies.
1245 *Front Pharmacol*. 13:897494. doi: 10.3389/fphar.2022.897494.

1246 Haji-Ghassemi, O., Y.S. Chen, K. Woll, G.B. Gurrola, C.R. Valdivia, W. Cai, S. Li, H.H. Valdivia, and F. Van
1247 Petegem. 2023. Cryo-EM analysis of scorpion toxin binding to Ryanodine Receptors reveals
1248 subconductance that is abolished by PKA phosphorylation. *Sci Adv*. 9:eadf4936. doi:
1249 10.1126/sciadv.adf4936.

1250 Hilser, V.J., J.O. Wrabl, and H.N. Motlagh. 2012. Structural and energetic basis of allostery. *Annu Rev*
1251 *Biophys*. 41:585-609. doi: 10.1146/annurev-biophys-050511-102319.

1252 Horrigan, F.T., and R.W. Aldrich. 2002. Coupling between voltage sensor activation, Ca2+ binding and
1253 channel opening in large conductance (BK) potassium channels. *J Gen Physiol*. 120:267-305. doi:
1254 10.1085/jgp.20028605.

1255 Iaparov, B., I. Baglaeva, I. Zahradnik, and A. Zahradnikova. 2022. Magnesium Ions Moderate Calcium-
1256 Induced Calcium Release in Cardiac Calcium Release Sites by Binding to Ryanodine Receptor
1257 Activation and Inhibition Sites. *Front Physiol*. 12:805956. doi: 10.3389/fphys.2021.805956.

1258 Ikemoto, N., and T. Yamamoto. 2000. Postulated role of inter-domain interaction within the ryanodine
1259 receptor in Ca(2+) channel regulation. *Trends Cardiovasc Med*. 10:310-316. doi:

1260 Imagawa, T., J.S. Smith, R. Coronado, and K.P. Campbell. 1987. Purified ryanodine receptor from skeletal
1261 muscle sarcoplasmic reticulum is the Ca2+ -permeable pore of the calcium release channel.
1262 *Journal of Biological Chemistry*. 262:16636-16643. doi:

1263 Iyer, K.A., V. Barnakov, and M. Samso. 2023. Three-dimensional perspective on ryanodine receptor
1264 mutations causing skeletal and cardiac muscle-related diseases. *Curr Opin Pharmacol*.
1265 68:102327. doi: 10.1016/j.coph.2022.102327.

1266 Iyer, K.A., Y. Hu, A.R. Nayak, N. Kurebayashi, T. Murayama, and M. Samso. 2020. Structural mechanism
1267 of two gain-of-function cardiac and skeletal RyR mutations at an equivalent site by cryo-EM. *Sci*
1268 *Adv*. 6:eabb2964. doi: 10.1126/sciadv.abb2964.

1269 Kobayashi, T., A. Tsutsumi, N. Kurebayashi, K. Saito, M. Kodama, T. Sakurai, M. Kikkawa, T. Murayama,
1270 and H. Ogawa. 2022. Molecular basis for gating of cardiac ryanodine receptor explains the
1271 mechanisms for gain- and loss-of function mutations. *Nat Commun*. 13:2821. doi:
1272 10.1038/s41467-022-30429-x.

1273 Kubalova, Z., D. Terentyev, S. Viatchenko-Karpinski, Y. Nishijima, I. Gyorke, R. Terentyeva, D.N. da Cunha,
1274 A. Sridhar, D.S. Feldman, R.L. Hamlin, C.A. Carnes, and S. Gyorke. 2005. Abnormal intrastore
1275 calcium signaling in chronic heart failure. *Proc.Natl.Acad.Sci U.S.A*. 102:14104-14109. doi:

1276 Laver, D.R., T.M. Baynes, and A.F. Dulhunty. 1997. Magnesium inhibition of ryanodine-receptor calcium
1277 channels: Evidence for two independent mechanisms. *J.Membrane.Biol*. 156:213-229. doi:

1278 Laver, D.R., C.H. Kong, M.S. Imtiaz, and M.B. Cannell. 2013. Termination of calcium-induced calcium
1279 release by induction decay: an emergent property of stochastic channel gating and molecular
1280 scale architecture. *J Mol Cell Cardiol*. 54:98-100. doi: 10.1016/j.yjmcc.2012.10.009.

1281 Laver, D.R., L.D. Roden, G.P. Ahern, K.R. Eager, P.R. Junankar, and A.F. Dulhunty. 1995. Cytoplasmic Ca2+
1282 inhibits the ryanodine receptor from cardiac muscle. *J.Membrane.Biol*. 147:7-22. doi:

1283 Lehnart, S.E., X.H. Wehrens, P.J. Laitinen, S.R. Reiken, S.X. Deng, Z. Cheng, D.W. Landry, K. Kontula, H.
1284 Swan, and A.R. Marks. 2004. Sudden death in familial polymorphic ventricular tachycardia
1285 associated with calcium release channel (ryanodine receptor) leak. *Circulation*. 109:3208-3214.
1286 doi:

1287 Li, J., M.S. Imtiaz, N.A. Beard, A.F. Dulhunty, R. Thorne, D.F. vanHelden, and D.R. Laver. 2013. ss-
1288 Adrenergic stimulation increases RyR2 activity via intracellular Ca2+ and Mg2+ regulation. *PLoS*
1289 *One*. 8:e58334. doi: 10.1371/journal.pone.0058334.

1290 Liu, W., D.A. Pasek, and G. Meissner. 1998. Modulation of Ca(2+)-gated cardiac muscle Ca(2+)-release
1291 channel (ryanodine receptor) by mono- and divalent ions. *American Journal of Physiology*.
1292 274:C120-C128. doi:

1293 Lu, C.H., C.C. Chen, C.S. Yu, Y.Y. Liu, J.J. Liu, S.T. Wei, and Y.F. Lin. 2022. MIB2: metal ion-binding site
1294 prediction and modeling server. *Bioinformatics*. 38:4428-4429. doi:
1295 10.1093/bioinformatics/btac534.

1296 Ma, J., K. Anderson, R. Shirokov, R. Levis, A. Gonzalez, M. Karhanek, M.M. Hosey, G. Meissner, and E.
1297 Rios. 1993. Effects of perchlorate on the molecules of excitation-contraction coupling of skeletal
1298 and cardiac muscle. *Journal of General Physiology*. 102:423-448. doi:

1299 Ma, R., O. Haji-Ghassemi, D. Ma, H. Jiang, L. Lin, L. Yao, A. Samurkas, Y. Li, Y. Wang, P. Cao, S. Wu, Y.
1300 Zhang, T. Murayama, B. Moussian, F. Van Petegem, and Z. Yuchi. 2020. Structural basis for
1301 diamide modulation of ryanodine receptor. *Nat Chem Biol*. 16:1246-1254. doi: 10.1038/s41589-
1302 020-0627-5.

1303 Marzen, S., H.G. Garcia, and R. Phillips. 2013. Statistical mechanics of Monod-Wyman-Changeux (MWC)
1304 models. *J Mol Biol*. 425:1433-1460. doi: 10.1016/j.jmb.2013.03.013.

1305 Meissner, G. 2017. The structural basis of ryanodine receptor ion channel function. *J Gen Physiol*.
1306 149:1065-1089. doi: 10.1085/jgp.201711878.

1307 Meissner, G., E. Rios, A. Tripathy, and D.A. Pasek. 1997. Regulation of skeletal muscle Ca2+ release
1308 channel (ryanodine receptor) by Ca2+ and monovalent cations and anions. *J.Biol Chem.*
1309 272:1628-1638. doi:

1310 Melville, Z., H. Dridi, Q. Yuan, S. Reiken, A. Wronska, Y. Liu, O.B. Clarke, and A.R. Marks. 2022a. A drug
1311 and ATP binding site in type 1 ryanodine receptor. *Structure*. 30:1025-1034 e1024. doi:
1312 10.1016/j.str.2022.04.010.

1313 Melville, Z., K. Kim, O.B. Clarke, and A.R. Marks. 2022b. High-resolution structure of the membrane-
1314 embedded skeletal muscle ryanodine receptor. *Structure*. 30:172-180 e173. doi:
1315 10.1016/j.str.2021.08.001.

1316 Miotto, M.C., G. Weninger, H. Dridi, Q. Yuan, Y. Liu, A. Wronska, Z. Melville, L. Sittenfeld, S. Reiken, and
1317 A.R. Marks. 2022. Structural analyses of human ryanodine receptor type 2 channels reveal the
1318 mechanisms for sudden cardiac death and treatment. *Sci Adv*. 8:eabo1272. doi:
1319 10.1126/sciadv.abo1272.

1320 Monod, J., J. Wyman, and J.P. Changeux. 1965. On the Nature of Allosteric Transitions: A Plausible
1321 Model. *J Mol Biol*. 12:88-118. doi: 10.1016/s0022-2836(65)80285-6.

1322 Murayama, T., N. Kurebayashi, T. Oba, H. Oyamada, K. Oguchi, T. Sakurai, and Y. Ogawa. 2011. Role of
1323 amino-terminal half of the S4-S5 linker in type 1 ryanodine receptor (RyR1) channel gating. *J Biol*
1324 *Chem*. 286:35571-35577. doi: 10.1074/jbc.M111.255240.

1325 Murayama, T., H. Ogawa, N. Kurebayashi, S. Ohno, M. Horie, and T. Sakurai. 2018. A tryptophan residue
1326 in the caffeine-binding site of the ryanodine receptor regulates Ca(2+) sensitivity. *Commun Biol*.
1327 1:98. doi: 10.1038/s42003-018-0103-x.

1328 Nayak, A.R., W. Rangubpit, A.H. Will, Y. Hu, P. Castro-Hartmann, J.J. Lobo, K. Dryden, G.D. Lamb, P.
1329 Sompornpisut, and M. Samso. 2024. Interplay between Mg(2+) and Ca(2+) at multiple sites of
1330 the ryanodine receptor. *Nat Commun*. 15:4115. doi: 10.1038/s41467-024-48292-3.

1331 Nayak, A.R., and M. Samso. 2022. Ca(2+) inactivation of the mammalian ryanodine receptor type 1 in a
1332 lipidic environment revealed by cryo-EM. *Elife*. 11. doi: 10.7554/eLife.75568.

1333 Niggli, E., N.D. Ullrich, D. Gutierrez, S. Kyrychenko, E. Polakova, and N. Shirokova. 2013. Posttranslational
1334 modifications of cardiac ryanodine receptors: Ca(2+) signaling and EC-coupling. *Biochim Biophys*
1335 *Acta*. 1833:866-875. doi: 10.1016/j.bbamcr.2012.08.016.

1336 Peng, W., H. Shen, J. Wu, W. Guo, X. Pan, R. Wang, S.R. Chen, and N. Yan. 2016. Structural basis for the
1337 gating mechanism of the type 2 ryanodine receptor RyR2. *Science*. 354. doi:
1338 10.1126/science.aah5324.

1339 Perez, C.F., S. Mukherjee, and P.D. Allen. 2003. Amino acids 1-1,680 of ryanodine receptor type 1 hold
1340 critical determinants of skeletal type for excitation-contraction coupling. Role of divergence
1341 domain D2. *J Biol Chem*. 278:39644-39652. doi: 10.1074/jbc.M305160200.

1342 Pettersen, E.F., T.D. Goddard, C.C. Huang, G.S. Couch, D.M. Greenblatt, E.C. Meng, and T.E. Ferrin. 2004.
1343 UCSF Chimera--a visualization system for exploratory research and analysis. *J Comput Chem*.
1344 25:1605-1612. doi: 10.1002/jcc.20084.

1345 Rios, E., and M.D. Stern. 1997. Calcium in close quarters: microdomain feedback in excitation-
1346 contraction coupling and other cell biological phenomena. *Annu.Rev.Biophys.Biomol.Struct.*
1347 26:47-82. doi:

1348 Robinson, R., D. Carpenter, M.A. Shaw, J. Halsall, and P. Hopkins. 2006. Mutations in RYR1 in malignant
1349 hyperthermia and central core disease. *Hum Mutat*. 27:977-989. doi: 10.1002/humu.20356.

1350 Sali, A., and T.L. Blundell. 1993. Comparative protein modelling by satisfaction of spatial restraints. *J Mol*
1351 *Biol*. 234:779-815. doi: 10.1006/jmbi.1993.1626.

1352 Samso, M. 2017. A guide to the 3D structure of the ryanodine receptor type 1 by cryoEM. *Protein Sci*.
1353 26:52-68. doi: 10.1002/pro.3052.

1354 Schneider, M.F., and B.J. Simon. 1988. Inactivation of calcium release from the sarcoplasmic reticulum in
1355 frog skeletal muscle. *J Physiol*. 405:727-745. doi: 10.1113/jphysiol.1988.sp017358.

1356 Sievers, F., A. Wilm, D. Dineen, T.J. Gibson, K. Karplus, W. Li, R. Lopez, H. McWilliam, M. Remmert, J.
1357 Soding, J.D. Thompson, and D.G. Higgins. 2011. Fast, scalable generation of high-quality protein
1358 multiple sequence alignments using Clustal Omega. *Mol Syst Biol*. 7:539. doi:
1359 10.1038/msb.2011.75.

1360 Sleiman, Y., A. Lacampagne, and A.C. Meli. 2021. "Ryanopathies" and RyR2 dysfunctions: can we further
1361 decipher them using in vitro human disease models? *Cell Death Dis*. 12:1041. doi:
1362 10.1038/s41419-021-04337-9.

1363 Sorrentino, V., and P. Volpe. 1993. Ryanodine receptors: how many, where and why?
1364 *Trends.Pharmacol.Sci.* 14:98-103. doi:

1365 Steele, T.W.E., and M. Samso. 2019. The FKBP12 subunit modifies the long-range allosterism of the
1366 ryanodine receptor. *J Struct Biol*. 205:180-188. doi: 10.1016/j.jsb.2018.12.007.

1367 Stern, M.D. 1992. Theory of excitation-contraction coupling in cardiac muscle. *Biophys J*. 63:497-517.
1368 doi: 10.1016/S0006-3495(92)81615-6.

1369 Stern, M.D., G. Pizarro, and E. Rios. 1997. Local control model of excitation-contraction coupling in
1370 skeletal muscle. *J Gen Physiol*. 110:415-440. doi: 10.1085/jgp.110.4.415.

1371 Tencerova, B., A. Zahradnikova, J. Gaburjakova, and M. Gaburjakova. 2012. Luminal Ca2+ controls
1372 activation of the cardiac ryanodine receptor by ATP. *J Gen Physiol*. 140:93-108. doi:
1373 10.1085/jgp.201110708.

1374 Uehara, A., T. Murayama, M. Yasukochi, M. Fill, M. Horie, T. Okamoto, Y. Matsuura, K. Uehara, T.
1375 Fujimoto, T. Sakurai, and N. Kurebayashi. 2017. Extensive Ca2+ leak through K4750Q cardiac
1376 ryanodine receptors caused by cytosolic and luminal Ca2+ hypersensitivity. *J Gen Physiol*.
1377 149:199-218. doi: 10.1085/jgp.201611624.

1378 Wagenknecht, T., and M. Samso. 2002. Three-dimensional reconstruction of ryanodine receptors. *Front*
1379 *Biosci*. 7:d1464-1474. doi: 10.2741/A853.

1380 Wang, J., A. Jain, L.R. McDonald, C. Gambogi, A.L. Lee, and N.V. Dokholyan. 2020. Mapping allosteric
1381 communications within individual proteins. *Nat Commun*. 11:3862. doi: 10.1038/s41467-020-
1382 17618-2.

1383 Wei, R., X. Wang, Y. Zhang, S. Mukherjee, L. Zhang, Q. Chen, X. Huang, S. Jing, C. Liu, S. Li, G. Wang, Y. Xu,
1384 S. Zhu, A.J. Williams, F. Sun, and C.C. Yin. 2016. Structural insights into Ca(2+)-activated long-
1385 range allosteric channel gating of RyR1. *Cell Res*. 26:977-994. doi: 10.1038/cr.2016.99.

1386 Wilson, A.D., J. Hu, C. Sigalas, E. Venturi, H.H. Valdivia, C.R. Valdivia, M. Lei, M. Musgaard, and R.
1387 Sitsapesan. 2021. The V2475F CPVT1 mutation yields distinct RyR2 channel populations that
1388 differ in their responses to cytosolic Ca(2+) and Mg(2). *J Physiol*. 599:5179-5201. doi:
1389 10.1113/JP281707.

1390 Wilson, M.A., and A.T. Brunger. 2000. The 1.0 A crystal structure of Ca(2+)-bound calmodulin: an
1391 analysis of disorder and implications for functionally relevant plasticity. *J Mol Biol*. 301:1237-
1392 1256. doi: 10.1006/jmbi.2000.4029.

1393 Witherspoon, J.W., and K.G. Meilleur. 2016. Review of RyR1 pathway and associated pathomechanisms.
1394 *Acta Neuropathol Commun*. 4:121. doi: 10.1186/s40478-016-0392-6.

1395 Woll, K.A., O. Haji-Ghassemi, and F. Van Petegem. 2021. Pathological conformations of disease mutant
1396 Ryanodine Receptors revealed by cryo-EM. *Nat Commun*. 12:807. doi: 10.1038/s41467-021-
1397 21141-3.

1398 Xiong, H., X. Feng, L. Gao, L. Xu, D.A. Pasek, J.H. Seok, and G. Meissner. 1998. Identification of a two EF-
1399 hand Ca2+ binding domain in lobster skeletal muscle ryanodine receptor/Ca2+ release channel.
1400 *Biochemistry*. 37:4804-4814. doi:

1401 Xu, L., G. Mann, and G. Meissner. 1996. Regulation of cardiac Ca2+ release channel (ryanodine receptor)
1402 by Ca2+, H+, Mg2+, and adenine nucleotides under normal and simulated ischemic conditions.
1403 *Circ Res*. 79:1100-1109. doi:

1404 Zahradnik, I., S. Gyorke, and A. Zahradnikova. 2005. Calcium activation of ryanodine receptor channels--
1405 reconciling RyR gating models with tetrameric channel structure. *J Gen Physiol*. 126:515-527.
1406 doi:

1407 Zahradnikova, A., M. Dura, I. Gyorke, A.L. Escobar, I. Zahradnik, and S. Gyorke. 2003. Regulation of
1408 dynamic behavior of cardiac ryanodine receptor by Mg2+ under simulated physiological
1409 conditions. *Am J Physiol Cell Physiol*. 285:C1059-1070. doi:

1410 Zahradnikova, A., B. Iaparov, and I. Zahradnik. 2020. The problem of accuracy in single-channel open
1411 probability measurements. *Prog Biophys Mol Biol*. 157:94-106. doi:
1412 10.1016/j.pbiomolbio.2020.05.002.

1413 Zahradnikova, A., I. Valent, and I. Zahradnik. 2010. Frequency and release flux of calcium sparks in rat
1414 cardiac myocytes: a relation to RYR gating. *J Gen Physiol*. 136:101-116. doi:
1415 10.1085/jgp.200910380.

1416 Zheng, W., and H. Wen. 2020. Investigating dual Ca(2+) modulation of the ryanodine receptor 1 by
1417 molecular dynamics simulation. *Proteins*. 88:1528-1539. doi: 10.1002/prot.25971.

1418 Zhou, Y., W. Yang, M. Kirberger, H.W. Lee, G. Ayalasomayajula, and J.J. Yang. 2006. Prediction of EF-hand
1419 calcium-binding proteins and analysis of bacterial EF-hand proteins. *Proteins*. 65:643-655. doi:
1420 10.1002/prot.21139.

1421 Ziman, A.P., C.W. Ward, G.G. Rodney, W.J. Lederer, and R.J. Bloch. 2010. Quantitative measurement of
1422 Ca(2)(+) in the sarcoplasmic reticulum lumen of mammalian skeletal muscle. *Biophys J*. 99:2705-
1423 2714. doi: 10.1016/j.bpj.2010.08.032.

1424